Circadian Control of Tumor Immunosuppression Impacts Efficacy of Immune Checkpoint Blockade

Bridget M. Fortin[1], **Shannon M. Pfeiffer**[1], **Jacob Insua-Rodríguez**[1,2], **Hamad Alshetaiwi**[3,4], **Alexander Moshensky**[2], **Wei A. Song**[1], **Alisa L. Mahieu**[1], **Sung Kook Chun**[1], **Amber N. Lewis**[1], **Alex Hsu**[1], **Isam Adam**[2], **Oliver S. Eng**[4,5], **Nicholas R. Pannunzio**[1,4,6,7], **Marcus M. Seldin**[1,4,7], **Ivan Marazzi**[1,4,7], **Francesco Marangoni**[2,4], **Devon A. Lawson**[2,4,7], **Kai Kessenbrock**[1,4,7], **Selma Masri**[1,4,7,#]

[1]Department of Biological Chemistry, University of California Irvine, Irvine, California, 92697, USA.

[2]Department of Physiology and Biophysics, University of California Irvine, Irvine, California, 92697, USA.

[3]Department of Pathology, University of Hail, Hail 2440, Saudi Arabia

[4]Chao Family Comprehensive Cancer Center, University of California Irvine, Irvine, California, 92697, USA.

[5]Department of Surgery, Division of Surgical Oncology, University of California Irvine, Orange, California, 92868, USA.

[6]Department of Medicine, Division of Hematology/Oncology, University of California Irvine, Irvine, California, 92697, USA.

[7]Center for Epigenetics and Metabolism, University of California Irvine, Irvine, California, 92697, USA.

Abstract

The circadian clock is a critical regulator of immunity, and this circadian control of immune modulation plays an essential role in host defense and tumor immunosurveillance. Using a single cell RNA-sequencing approach in a genetic model of colorectal cancer (CRC), we identified clock-dependent changes to the immune landscape that dictate the abundance of immunosuppressive cells and consequent suppression of cytotoxic CD8$^+$ T cells. Of these immunosuppressive cell types, PD-L1 expressing myeloid-derived suppressor cells (MDSCs) peak in abundance in a rhythmic manner. Mechanistically, we identified that disruption of the epithelial

cell clock regulates the secretion of cytokines that promote heightened inflammation, recruitment of neutrophils, and the subsequent development of MDSCs. We leveraged these findings to demonstrate that time-of-day anti-PD-L1 delivery is most effective when synchronized with the abundance of immunosuppressive MDSCs. Collectively, our results indicate that circadian gating of tumor immunosuppression informs the timing and efficacy of immune checkpoint inhibitors (ICIs).

One-Sentence Summary:

Immunosuppression is regulated by the circadian clock and can be leveraged to promote the efficacy of immune checkpoint inhibitor therapy.

INTRODUCTION

Colorectal cancer (CRC) represents a significant health challenge globally, with high morbidity and mortality rates that are rising in young adults[1–4]. The current standard of care for CRC relies on 5-Fluorouracil-based chemotherapy that lacks specificity and is associated with significant toxicity[5–8]. Immunotherapy has emerged as a promising approach for the treatment of multiple cancer types[9–11]. Although ICIs have demonstrated efficacy in patients with advanced, microsatellite instability high CRC[12,13], which is known for its pronounced immunogenicity, the majority of CRC cases remain unresponsive. Also, even among cancers that are highly responsive to immunotherapy, a majority of patients demonstrate disease progression on ICI therapy[14,15]. Thus, these findings represent a significant clinical hurdle in the treatment of solid tumors and underscore the need to improve the efficacy of ICIs.

The circadian clock is the biological timekeeping mechanism that governs endocrine, metabolic, and immune functions to maintain physiological homeostasis[16–20]. The clock impinges on innate immunity by regulating time-of-day dependent production and trafficking of cytokines/chemokines, as well as immune cell maturation and tissue infiltration[21–24]. In particular, myeloid cell-specific deletion of *Bmal1* was shown to abrogate the rhythmic cycling of monocytes and promote the accumulation of inflammatory Ly6C^{hi} monocytes in non-tumor models[25,26]. While these studies establish a causal link between the circadian clock and innate immunity, less is known regarding how the clock impacts anti-tumor immunity. Using a MMTV:PyMT breast cancer model and xenograft model of melanoma, the abundance and function of tumor-antigen specific CD8$^+$ T cells was found to be clock-controlled, and regulated by dendritic cells (DCs)[27,28]. However, whether the activity of cytotoxic CD8$^+$ T cells is also dependent on clock-controlled regulation of immunosuppression remains mechanistically undefined.

Chronomedicine suggests that the timing of delivery of cancer therapeutics can significantly impact treatment outcome. In support of this, studies have provided compelling evidence that morning administration of chemotherapy can mitigate side effects and enhance treatment response across diverse cancer types[29–31]. Preclinical models and early stage clinical trials have also demonstrated increased efficacy of cytokine infusions in a time-of-day-dependent manner[32–37]. In terms of delivery timing of ICIs, studies are limited with the exception of retrospective analyses of multiple tumor types where afternoon dosing of

ICIs was significantly associated with shorter overall survival[38–41]. Notably, immunotherapy agents exhibit rapid, partial tissue-clearance within 12 hours after administration[42], indicating that the timing of treatment could be critical for stimulating anti-tumor immunity.

Here, we show that the clock impinges on tumor immunosuppression which dictates optimal timing of ICIs. Using a genetic model of CRC, we utilized a single-cell RNA-sequencing (scRNA-seq) approach and identified clock-dependent control of the immune landscape within the tumor microenvironment. Genetic and environmental disruption of the circadian clock resulted in accumulation of MDSCs and a decrease in cytotoxic CD8$^+$ T cells. More specifically, we identified an important signaling axis between the intestinal epithelial circadian clock and immune cells through the secretion of proinflammatory cytokines and chemokines. Given the role of the circadian network in regulating immunity, the abundance of PD-L1 expressing MDSCs was found to be rhythmic in the intestine and in peripheral tissues. Finally, we leveraged these data to show that anti-PD-L1 administration was most effective in the early active phase of mice when immunosuppressive MDSCs were more abundant. Our results demonstrate that clock-dependent control of anti-tumor immunity can inform the optimal timing and efficacy of immune checkpoint blockade.

RESULTS

Clock disruption alters the immune landscape

A growing body of evidence suggests a critical link between circadian clock dysregulation and multiple different types of cancer[27,43–55]. We previously reported that clock disruption promotes tumor progression in an *Apc*-driven model of CRC[53]. Our genetically engineered mouse model (GEMM) harbors both intestine-specific knockout of *Bmal1*, to disrupt the clock, and heterozygous deletion of *Apc*, to initiate CRC (Figure S1A–B). *Apc* and *Bmal1* were selectively deleted in intestinal epithelial cells (*Apc*$^{+/\ ex1-15}$;*Bmal1*$^{fl/fl}$;*Villin-Cre*) using Villin-Cre, and we denote *Bmal1*$^{fl/fl}$;*Villin-Cre* mice as <u>*Bmal1*$^{-/-}$</u>, *Apc*$^{+/\ ex1-15}$;*Villin-Cre* mice as <u>*Apc*$^{+/-}$</u>, and *Apc*$^{+/\ ex1-15}$;*Bmal1*$^{fl/fl}$;*Villin-Cre* mice as <u>*Apc*$^{+/-}$;*Bmal1*$^{-/-}$</u>. Importantly, in the *Bmal1*$^{-/-}$ and *Apc*$^{+/-}$;*Bmal1*$^{-/-}$ mice, the clock is only disrupted in intestinal epithelial cells and remains intact in the periphery, thus establishing a system to delineate the crosstalk between the intestinal epithelial clock and the immune system. Furthermore, defining this axis is critical for advancing our understanding of time-of-day control of anti-tumor immunity.

Using this GEMM of CRC, we previously reported the impact of clock disruption on tumor burden and pathological features[53]. Consistent with previous findings[56], intestinal hematoxylin/eosin (H&E) sections from *Apc*$^{+/-}$ mice contained early neoplastic precursor lesions and tubular adenomas[53]. In contrast, *Apc*$^{+/-}$;*Bmal1*$^{-/-}$ mice showed a striking increase in neoplastic changes, ranging from tubular adenomas to locally invasive adenocarcinomas extending into the muscularis propria[53]. Additionally, polyp count, which includes early neoplastic precursor lesions, tubular adenomas, and locally invasive adenocarcinomas, was used to quantify tumor burden. *Apc*$^{+/-}$;*Bmal1*$^{-/-}$ mice were found to have significantly greater intestinal polyp count versus *Apc*$^{+/-}$ mice (Figure S1C). Spleen weight was also significantly elevated in *Apc*$^{+/-}$;*Bmal1*$^{-/-}$ mice compared to *Apc*$^{+/-}$ mice (Figure S1D), suggesting increased systemic inflammation in clock mutant, tumor-

bearing mice. Together, these data link disruption of the circadian clock in the intestine to acceleration of CRC progression.

The circadian clock has been linked with immunity through time-of-day dependent regulation of cytokine/chemokine production, as well as the release and trafficking of immune cells to target tissues[21,22,24,55,57]. However, how circadian clock disruption in intestinal epithelial cells regulates tissue-specific and systemic control of anti-tumor immunity is unknown. Therefore, to define the impact of clock disruption on the immune landscape in the intestine, we performed scRNA-seq with CD45^{+} sorted immune cells isolated at Zeitgeber time (ZT) 4 from WT, *Bmal1*^{−/−}, *Apc*^{+/−}, and *Apc*^{+/−}*;Bmal1*^{−/−} mice (Figure 1A). Based on UMAP clustering and analyses of immune cell lineage marker expression (Figures S1E–F, Figure S2A), scRNA-seq identified distinct clusters of myeloid and lymphoid cells. These cells included neutrophils (*S100a8, S100a9, Cxcr2*), monocytes/ macrophages/dendritic cells (DCs) (*C1qa, C1qb, Fn1*), mast cells (*Kit*), CD8^{+} T cells (*CD8a, Gzma, Ccl5*), CD4^{+} T cells (*CD4, Ms4a4b, Trbc2*), double-negative (DN) T cells (*Ms4a4b, Trbc2,* low for *CD4* and *CD8a*), innate lymphoid cells (ILCs) (*Il7r, Gata3, Klrg1*), naïve B cells (*CD19, Ms4a1, CD79a*), mature B cells (*Jchain, Igha, Igkc*), and proliferating B cells (*Mki67, Top2a, Pclaf*) (Figure 1B). Immune cell populations that were clock-dependent or tumor-specific were analyzed further. Notably, scRNA-seq revealed differences in the immune landscape in the *Bmal1*^{−/−}, *Apc*^{+/−}, and *Apc*^{+/−}*;Bmal1*^{−/−} mice compared to WT (Figure 1B–E). Importantly, clock disruption alone, in the absence of cancer initiation, also altered the immune landscape. When compared to WT, *Bmal1*^{−/−}, *Apc*^{+/−}, and *Apc*^{+/−}*;Bmal1*^{−/−} mice had increased proportions of neutrophils as well as decreased proportions of CD8^{+} T cells, with less of an impact on monocytes/macrophages, DCs, B cells, CD4^{+} T cells, and CD25^{+} T cells (Figure 1D–E, Figure S2B–D). Based on total numbers of myeloid and lymphoid cells, the most striking difference was an increase in the number of neutrophils in the *Bmal1*^{−/−}, *Apc*^{+/−}, and *Apc*^{+/−}*;Bmal1*^{−/−} mice (Figure 1D–E, Figure S2C). This increase in neutrophils in the clock-disrupted mice suggests that neutrophils could be a potential driver of these immune alterations.

Also, multiple B cell clusters were identified in the scRNA-seq data, including naïve B cells, mature B cells, and proliferating B cells (Figure 1D, S2D–E), consistent with the literature differentiating these B cell subtypes[58–62]. Interestingly, the count of naïve B cells decreased while mature B cells increased only in the tumor-bearing *Apc*^{+/−} and *Apc*^{+/−}*;Bmal1*^{−/−} mice, and this was independent of clock disruption (Figure 1D, S2D–E). Based on published reports, cancer development promotes tumor infiltration of B cells that alters their cell surface marker expression, identity, and function, thus resulting in increased B cell heterogeneity[62–64]. These findings are consistent with our scRNA-seq data illustrating a tumor-specific role for remodeling of B cells.

Clock disruption promotes immune microenvironment remodeling

To further define changes to the immune landscape following clock disruption, a flow cytometry panel was established to quantify immune cell types within the intestine and spleen (Figure S3A). Both panels included a marker to gate live cells as well as CD45 for sorting bulk immune cells. The myeloid panel included CD11b for myeloid cells,

F4/80 for macrophages, Ly6C for monocytes, and Ly6G for neutrophils. The lymphocyte panel included CD3 for T cells, CD4 for CD4$^+$ T cells, CD8 for CD8$^+$ T cells and CD25 for CD25$^+$ T cells. These mice were separated to profile the impact of the clock in the absence (WT and *Bmal1$^{-/-}$*) and presence (*Apc$^{+/-}$* and *Apc$^{+/-}$;Bmal1$^{-/-}$*) of a tumor microenvironment, as we expect greater immune cell changes during cancer progression. Importantly, clock disruption did not alter the total frequency of intestinal CD45$^+$ immune cells (Figure S4A). Both *Bmal1$^{-/-}$* and *Apc$^{+/-}$;Bmal1$^{-/-}$* mice had significantly higher proportions of neutrophils and monocytes, as well as significantly reduced proportions of CD8$^+$ T cells (Figure 2A–B, Figure S4B–E). Of these changes, the increase in neutrophils was the most prominent, with a 5-fold increase in the *Bmal1$^{-/-}$* intestine compared to WT and a 5-fold increase in the *Apc$^{+/-}$;Bmal1$^{-/-}$* intestine compared to *Apc$^{+/-}$* (Figure 2A–B). This suggests that clock disruption promotes an increase in neutrophils in both non-tumor-bearing and tumor-bearing microenvironments. The proportions of total CD3$^+$ T cells, CD4$^+$ T cells, and CD25$^+$ T cells in the intestine were unaffected by clock disruption (Figure S5A). Spleens isolated from *Bmal1$^{-/-}$* and *Apc$^{+/-}$;Bmal1$^{-/-}$* mice also had significantly higher proportions of neutrophils and monocytes (Figure S5B). We also profiled the abundance of macrophages and CD25$^+$ T cells in both the intestine and spleen and did not observe a consistent clock-dependent effect (Figure 2A–B, Figure S5A–B). These flow cytometry data suggest that clock disruption in intestinal epithelial cells significantly increased the abundance of neutrophils in tumor-bearing and non-tumor-bearing mice, which is corroborated by our scRNA-seq analysis.

In humans, circadian rhythms are frequently disrupted by environmental stimuli including night shift work, jet lag, and extended light-at-night exposure[65–67], and several of these environmental disruption paradigms have been shown to accelerate cancer progression in mice[27,44,45,48,50,53,68]. Therefore, in order to define whether environmental clock disruption mirrors the alterations to the immune landscape seen with genetic clock disruption, WT mice were exposed to an established environmental shift paradigm that models jet lag and night shift work 3–4 times/week for 8 weeks (Figure 2C)[27,50,53,69,70]. We previously used this paradigm and demonstrated a significant loss of rhythmicity of the respiratory exchange ratio, locomotor activity, and food intake, signifying a systemic disruption of the circadian clock[53]. Shift disruption (SD) significantly increased proportions of neutrophils, monocytes, and macrophages, and resulted in a significant reduction in CD8$^+$ T cells in the intestine (Figure 2D). Neither genetic clock disruption alone (Figure S1D) nor environmental clock disruption (Figure S5C) led to an increase in spleen weight that is seen in the tumor-bearing mice (Figure S1D). This suggests that tumor progression is necessary for spleen enlargement. Lastly, SD led to a significant reduction in the proportion of CD4$^+$ T cells (Figure S5D), likely because environmental clock disruption impacts rhythmicity in both intestinal epithelial cells and immune cells systemically. Taken together, data from our environmental paradigm corroborate findings from the genetic clock mutant model and demonstrate that clock disruption alters immune cell frequency, both systemically and locally within the intestine.

Importantly, genetic and environmental clock disruption were found to alter proportions of both myeloid and lymphoid cells (Figure 2A–D). To determine which cell type was initially impacted by circadian clock disruption, WT mice were exposed to an SD time-course for

1 week, 3 weeks, or 5 weeks and flow cytometry was subsequently used to track changes to the immune landscape. Similar to mice exposed to 8 weeks of the SD paradigm (Figure S5C), spleen weight was unaffected by short-term SD exposure (Figure S5E). However, SD led to a significant increase in the proportion of neutrophils after only 3 weeks (Figure 2E–F). This was followed by an increase in the proportion of monocytes and macrophages and a reduction in the proportion of CD8$^+$ T cells after 5 weeks of environmental shift (Figure 2F). The proportion of CD4$^+$ T cells was unaffected after 5 weeks of SD (Figure S5F) and reduced only after 8 weeks of shift (Figure S5D), demonstrating that abundance of CD4$^+$ T cells is not initially changed following circadian clock disruption. These data suggest that environmental clock disruption triggers an initial alteration in neutrophil proportions prior to secondary immune cell adaptations including a reduction in cytotoxic CD8$^+$ T cells.

Disruption of the clock promotes MDSC accumulation

Our data suggest that clock disruption plays an important role in regulating immune cell proportions in CRC, yet how this influences cancer progression remains undefined. Interestingly, genetic knockout of *Bmal1* alone resulted in a pronounced decrease in intestinal cytotoxic CD8$^+$ T cells (Figure 1D–E, Figure 2A), suggesting that the circadian clock is involved in immunosuppression. Our scRNA-seq identified a cluster of myeloid cells, mainly neutrophils, that highly expressed markers of MDSCs including *Ifitm1, Wfdc17, S100a8, S100a9, Irg1*, and *Arg2* (Figure S6A). This neutrophilic population is enriched as a result of both clock disruption and cancer (Figure S6B). MDSCs, often neutrophil- and monocyte- derived, have been reported to suppress cytotoxic CD8$^+$ T cell proliferation and activity[71–74], and recent evidence suggests that increased accumulation of neutrophils can induce immunosuppression and tumor progression[28,75–78].

To further define this, putative MDSCs were sorted by flow cytometry from intestines and spleens of WT, *Bmal1*$^{-/-}$, *Apc*$^{+/-}$, and *Apc*$^{+/-}$;*Bmal1*$^{-/-}$ mice (Figure 3A, Figure S3B). Importantly, these mice were separated to profile the impact of clock disruption in non-tumor-bearing versus tumor-bearing microenvironments. MDSCs consist of two major subsets of Ly6G$^+$Ly6C^{low} granulocytic and Ly6G$^-$Ly6C^{high} monocytic cells[79–81]. Thus, CD11b, a marker for myeloid cells, and Gr1, a marker for both Ly6C and Ly6G, were used to sort both monocytes and neutrophils, the most common populations comprising MDSCs[79–81]. Both *Bmal1*$^{-/-}$ and *Apc*$^{+/-}$;*Bmal1*$^{-/-}$ mice had significantly greater proportions of Gr1$^+$ cells (Figure 3B–D). MDSCs can suppress T cells through the generation of reactive oxygen species (ROS)[71,82]. To determine if the production of ROS is influenced by clock disruption, we used cell permeable reagent 2',7'–dichlorofluorescin diacetate (H$_2$DCFDA), which becomes fluorescent in the presence of ROS, to quantitatively measure ROS accumulation in the mouse intestine. Gr1$^+$ cells from *Bmal1*$^{-/-}$ and *Apc*$^{+/-}$;*Bmal1*$^{-/-}$ mice exhibited greater levels of ROS (Figure 3E–F). An additional mechanism of T cell suppression is the upregulation of PD-L1 by MDSCs[83–85]. A greater percentage of Gr1$^+$ cells from *Bmal1*$^{-/-}$ and *Apc*$^{+/-}$;*Bmal1*$^{-/-}$ mice were also found to be PD-L1$^+$ (Figure 3G–H), suggesting these MDSCs could be immunosuppressive. Similarly, gene expression analysis of splenic Gr1$^+$ cells revealed a significant upregulation of immunosuppressive genes including *S100a8, S100a9, and Wfdc17* in the *Bmal1*$^{-/-}$ and *Apc*$^{+/-}$;*Bmal1*$^{-/-}$ mice

(Figure 3I–J). These data demonstrate that clock disruption, even in the absence of a tumor microenvironment, promotes the accumulation of immunosuppressive myeloid cells.

To confirm the immunosuppressive ability of these putative MDSCs at the functional level, a classical T cell suppression assay was performed. This assay involved activating naïve T cells with CD3/CD28 and staining with a proliferation dye eFluor670 that is diluted as a result of consecutive cell divisions. Next, activated T cells were co-cultured with Gr1$^+$ cells isolated from WT, *Bmal1*$^{-/-}$, *Apc*$^{+/-}$, and *Apc*$^{+/-}$;*Bmal1*$^{-/-}$ mice. After 3 days of co-culture, flow cytometry was used to measure the counts of CD4$^+$ and CD8$^+$ T cells as well as the proportion of these cells that maintained the proliferation dye, allowing for a quantification of T cell proliferation and a readout for immunosuppression (Figure S3C). We found that MDSCs from clock-disrupted *Bmal1*$^{-/-}$, and tumor-bearing *Apc*$^{+/-}$ and *Apc*$^{+/-}$;*Bmal1*$^{-/-}$ mice, significantly suppressed T cell proliferation (Figure 3K, Figure S6C–D). Our findings suggest that immunosuppression is likely mediated through clock-dependent control of MDSCs in a model of CRC.

Clock disruption drives a Wnt-mediated inflammatory response

To define the underlying molecular mechanism of immune cell remodeling, we further dissected the role of the circadian clock in the intestinal epithelium. Importantly, Wnt signaling regulates development, proliferation, and stemness and is an essential pathway for maintaining homeostasis in the intestine[86]. We have previously shown that *Bmal1* loss promotes *Apc* loss of heterozygosity by increasing genome instability and resulting in hyperactivation of Wnt signaling[53]. A key Wnt-target gene, *c-Myc*, has also been shown to regulate inflammation and immunosuppression within the tumor microenvironment[87–91]. Taken together, these findings suggest that the circadian clock and Wnt signaling could converge to regulate inflammation and subsequent remodeling of the intestinal immune landscape.

To test this, the primary intestinal epithelium was isolated from mice and plated to establish monolayer cultures as well as routinely used intestinal organoid models, both of which recapitulate the cell identity found in the intestine[92–94]. WT and *Bmal1*$^{-/-}$ intestinal monolayers and organoids were treated with recombinant mouse Wnt3a to define the Wnt-dependent transcriptional response in the absence and presence of a functional clock. Intestinal *Bmal1*$^{-/-}$ led to an upregulation of MYC protein, which was further heightened in the presence of Wnt3a treatment (Figure 4A, Figure S7A). Compared to WT, Wnt target genes *c-Myc* and *Survivin* were significantly upregulated in *Bmal1*$^{-/-}$ intestinal monolayers in a Wnt3a-dependent manner (Figure 4B). Similar results were obtained using WT and *Bmal1*$^{-/-}$ intestinal organoids treated with either recombinant mouse Wnt3a or Wnt3a conditioned media (CM) (Figure S7B–C). Strikingly, the inflammatory cytokine *Cxcl5* was also upregulated in a Wnt-dependent manner, and this response was significantly enhanced upon intestinal clock disruption (Figure 4B, S7B–C). Together, these data highlight a potential role for Wnt signaling and the circadian clock in regulating inflammation. Therefore, we propose that clock disruption and Wnt signaling coordinately promote a heightened pro-inflammatory response to recruit myeloid cells, including neutrophils, within the intestinal epithelium (Figure 4C).

To delineate the pro-inflammatory roles of the clock and Wnt signaling, WT and $Bmal1^{-/-}$ primary intestinal monolayers were treated with and without recombinant Wnt3a and a 32-plex mouse cytokine/chemokine array was performed. Importantly, both clock-dependent and Wnt-dependent increases in cytokine production were identified in both cell lysate and CM. IL-5, CCL5, IL-17, and CXCL9 were found to be exclusively clock-dependent as these cytokines were significantly upregulated in $Bmal1^{-/-}$ intestinal monolayers compared to WT (Figure 4D and G, Figure S7D). CCL5, IL-17, and CXCL9 were found to be significantly upregulated in mice during chronic intestinal inflammation and cancer, leading to the recruitment of neutrophils[95–101]. IL-17 promotes neutrophil expansion and survival as well as the production of immune-suppressive molecules $s100a8$ and $s100a9$[102–108]. Collectively, these data suggest that clock disruption promotes a pro-inflammatory response in intestinal epithelial cells that could drive a myeloid-dependent immunosuppressive phenotype.

In addition to clock-dependent changes in cytokine regulation, additional cytokines and chemokines were identified to be exclusively Wnt-dependent. These include CXCL1, M-CSF, G-CSF, GM-CSF, CCL2, IL-2, VEGF, TNFα, and IFNγ (Figure 4E, 4G, Figure S7E), which all have pro-inflammatory roles[109]. Additionally, CXCL5, CXCL6, and CXCL2 were identified to be both clock and Wnt-dependent (Figure 4F–G, Figure S8A). These cytokines are also known to be activated during an inflammatory response and consequently function as neutrophil chemoattractants[21,110–116]. To confirm our findings in an additional cell model, mouse embryonic fibroblasts (MEFs) were similarly treated with recombinant Wnt3a which resulted in a significant upregulation of the Wnt target genes c-Myc, $Survivin$, and $Axin2$, as well as the inflammatory cytokines $Cxcl5$, $Cxcl1$, M-csf, and Gm-csf (Figure S8B). Similar to intestinal organoids, $Cxcl5$ was the most highly upregulated cytokine, with an over 100-fold induction in response to Wnt3a (Figure S8B). Finally, to define transcriptional control of inflammatory cytokines, knockdown of MYC was performed in primary intestinal monolayers. MYC knockdown resulted in a significant downregulation of $Cxcl5$ gene expression (Figure S8C). These data suggest that MYC is at least partially involved in the Wnt-dependent transcriptional control of the pro-inflammatory cytokine $Cxcl5$.

Clock disruption promotes neutrophil migration and suppression

We identified multiple pro-inflammatory and potentially immunosuppressive cytokines that are both clock and Wnt-dependent (Figure 4D–G). However, the functional consequence of these cytokines and chemokines on neutrophil identity, gene expression, and migration remained undefined. To test this, WT and $Bmal1^{-/-}$ primary intestinal monolayers were treated with recombinant Wnt3a and CM was collected, to define the role of the clock and Wnt signaling on neutrophil phenotype and function. Next, naïve bone marrow-derived neutrophils isolated from WT mice were incubated with CM from WT and $Bmal1^{-/-}$ intestinal monolayers that we have shown to secrete several pro-inflammatory cytokines and chemokines (Figure 4D–G). Notably, only neutrophils cultured with CM collected from $Bmal1^{-/-}$ intestinal monolayers exhibited a Wnt-dependent upregulation of MDSC-signature genes including $s100a8$, $s100a9$, $Wfdc17$, and $Arg2$ (Figure 4H). Additionally, naïve bone marrow-derived neutrophils were isolated from WT mice and placed into transwell chambers to assess chemotaxis toward cytokine/chemokine enriched CM. Primary

neutrophils were incubated with CM from WT and $Bmal1^{-/-}$ intestinal monolayers, and a significant proportion of neutrophils were migratory in the presence of CM from $Bmal1^{-/-}$ primary intestinal epithelium (Figure 4I). These data demonstrate that clock disruption and Wnt activation promoted an immunosuppressive neutrophil phenotype as well as increased neutrophil migration.

Accumulation of PD-L1⁺ myeloid cells in human CRC

To determine the physiological relevance of our findings, we analyzed the immune populations of normal human colon versus CRC tumors from 36 patients profiled by scRNA-seq[117]. We focused solely on CD45⁺ immune cells and classified naïve B cells, mature B cells, T cells, NK cells, and myeloid cells based on UMAP clustering and immune cell lineage marker expression (Figure S9A–B). We found that myeloid cells were highly abundant in human CRC samples when compared to patient-matched normal colon (Figure S9C–D). Importantly, consistent with previous literature[118,119], PD-L1 was found to be highly expressed by this myeloid cluster and expression was increased in CRC samples relative to normal colon (Figure S9E–F). These data suggest that PD-L1⁺ myeloid cells are highly abundant in human CRC, and this potentially immunosuppressive cell population could be therapeutically targetable.

Time of day anti-PD-L1 treatment determines efficacy

Utilizing our mouse scRNA-seq dataset, we assessed the expression level of PD-L1 and found that it was highly enriched in myeloid cells, and specifically neutrophils (Figure S10A–D). Importantly, the expression of PD-L1 was increased in the $Bmal1^{-/-}$, $Apc^{+/-}$, and $Apc^{+/-};Bmal1^{-/-}$ mice (Figure S10C–E). Together, these data suggest that neutrophils highly express PD-L1 and that clock disruption could be integral in driving this upregulation. Therefore, to define if immunosuppressive MDSCs and PD-L1 expression are regulated by the circadian clock, mice were sacrificed during the early rest phase (ZT 4) and during the early active phase (ZT 16). Flow cytometry was used to assess the proportion of Gr1⁺ and PD-L1⁺ cells in the intestine and peripheral tissues. Intestinal polyps and spleen weight were not significantly different between $Apc^{+/-};Bmal1^{-/-}$ mice in the ZT 4 group compared to ZT 16 (Figure S10F–G). Of importance, the circadian clock in $Apc^{+/-};Bmal1^{-/-}$ mice is disrupted in intestinal epithelial cells and remains intact in other organs. In WT mice, there is a significant increase in the proportion of Gr1⁺ and Gr1⁺PD-L1⁺ cells in the intestine at ZT 16 compared to ZT 4 (Figure 5A–B). In contrast, this rhythm of Gr1⁺ and Gr1⁺PD-L1⁺ cells is lost in the intestine of $Apc^{+/-};Bmal1^{-/-}$ mice (Figure 5A–B). In the spleen, where the circadian clock remains intact, we identified a significant increase in Gr1⁺ and Gr1⁺PD-L1⁺ cells at ZT 16 in both WT and $Apc^{+/-};Bmal1^{-/-}$ mice (Figure 5C–D). Gr1⁺ and Gr1⁺PD-L1⁺ cells were also profiled in mesenteric tumor-draining lymph node (mLN) and blood, but absolute levels were low compared to the intestine and spleen (Figure S10H–I). We quantified cumulative levels of Gr1⁺ and Gr1⁺PD-L1⁺ cells in both the intestine and spleen, the organs with the greatest proportions of these MDSCs. There were significantly more Gr1⁺ and Gr1⁺PD-L1⁺ cells at ZT 16 compared to ZT 4 (Figure S10J–K), indicating that immunosuppressive myeloid cells peak during the early active phase. Altogether, these data demonstrate that the abundance of Gr1⁺ MDSCs, as well as the expression of PD-L1, is

rhythmic and conceptually establishes a framework for time-of-day treatment of anti-PD-L1 immunotherapy.

In order to assess the translational potential of our findings, $Apc^{+/-};Bmal1^{-/-}$ mice were treated twice a week with anti-PD-L1 at either ZT 4 or ZT 16 for 3 weeks. We hypothesized that targeting these immunosuppressive MDSCs with anti-PD-L1 at ZT 16, when $Gr1^+PD-L1^+$ cells are most abundant, would provide greater anti-tumor efficacy. After treatment, tumor burden and spleen weight were assessed and flow cytometry was used to determine the proportions of $Gr1^+$ cells and $CD8^+$ T cells (Figure 5E). Importantly, spleen weight was increased in $Apc^{+/-};Bmal1^{-/-}$ mice treated at ZT 16 and not in $Apc^{+/-};Bmal1^{-/-}$ mice treated at ZT 4 (Figure 5F), demonstrating that the inflammatory response generated by anti-PD-L1 is dependent on time-of-day delivery. Also, unlike anti-PD-L1 treatment at ZT 4, anti-PD-L1 treatment at ZT 16 significantly reduced intestinal $Gr1^+$ cells in $Apc^{+/-};Bmal1^{-/-}$ mice (Figure 5G). Treatment of $Apc^{+/-};Bmal1^{-/-}$ mice with anti-PD-L1 at ZT 16 was found to promote a greater increase in intestinal $CD8^+$ T cells compared to ZT 4 treatment (Figure 5H), suggesting a more robust anti-tumor immune response generated upon treatment in the early active phase. Though anti-PD-L1 treatment did not significantly decrease intestinal polyp count after only 3 weeks (Figure S10L), it significantly reduced polyp size in $Apc^{+/-};Bmal1^{-/-}$ mice when administered at ZT 16, the time when $Gr1^+PD-L1^+$ cells are most abundant (Figure 5I).

In addition to our GEMM of CRC, we also performed time of day anti-PD-L1 administration in subcutaneous models of CRC (MC38), lung cancer (CMT167), and melanoma (D4M-S), which are known to respond to immunotherapy[120–125]. Both ZT 4 and ZT 16 administration of anti-PD-L1 significantly reduced MC38 tumor growth over time (Figure 5J) and tumor size (Figure 5K). Complete response (CR), where no tumor could be detected, and progressive disease (PD), where the treatment had no effect on tumor growth, were calculated for the MC38 tumor model at the end of the experiment. CR was observed for 1/12 (8%) tumors with ZT 4 treatment versus 4/14 (30%) tumors with ZT 16 treatment (Figure 5J–K). PD was observed for 6/12 (50%) tumors with ZT 4 treatment versus 4/14 (29%) tumors with ZT 16 treatment (Figure 5J–K). Importantly, the CMT167 lung cancer line was less responsive to immunotherapy, however, a significant reduction in tumor volume was observed when anti-PD-L1 was administered only at ZT 16 (Figure 5L, Figure S10M). Finally, our data show that the D4M-S melanoma line is highly responsive to immunotherapy, and ZT 16 administration of anti-PD-L1 was more effective at reducing tumor growth (Figure 5M, Figure S10N). Taken together, these findings demonstrate that time-dependent regulation of $PD-L1^+$ MDSCs can be harnessed to promote the efficacy of immune checkpoint blockade in the treatment of CRC, as well as lung cancer and melanoma (Figure 6).

DISCUSSION

Circadian control of innate immunity plays a critical role in regulating the trafficking and recruitment of myeloid cells, such as monocytes, macrophages, and neutrophils, which are essential components for host defense[21,24–26,78,126,127]. Additionally, tumor immunosurveillance has recently emerged as a dynamic process that also displays

rhythmicity over the day/night cycle. Specifically, the rhythmic trafficking and function of DCs that governs tumor antigen presentation and subsequent priming of cytotoxic CD8^{+} T cells controls tumor growth[28], and likely also governs rhythmic metastatic dissemination[27,128]. In addition to DC-dependent antigen processing by the circadian clock, it has been reported that efficacy of vaccination is time-of-day dependent in both tumor and non-tumor models[28,126]. Therefore, we reasoned that the circadian clock likely dictates additional unknown factors that impinge on anti-tumor immunity, which could also inform therapeutic efficacy of immune checkpoint blockade.

Utilizing an unbiased scRNA-seq approach, we identified clock-dependent changes to the tumor immune landscape that govern immunosuppression. Mechanistically, our data support a model where an inherent crosstalk exists between epithelial and immune cells that is guided by the circadian clock network in the intestine. Disruption of the intestinal epithelial cell clock resulted in hyperactivation of pro-inflammatory cytokines and chemokines that promote neutrophil accumulation, MDSC development, and immunosuppression. Given that the intestinal epithelium is highly Wnt-responsive, and clock disruption hyperactivates intestinal Wnt signaling (Figure 4)[53], our data reveal a host of pro-inflammatory factors that are Wnt-dependent, clock-dependent, or reliant on both pathways. Additionally, previous clinical studies have shown that in patients, MDSC accumulation is associated with advanced stage and metastatic CRC[118,119]. Our work now uncovers a previously unknown mechanism of MDSC control that is coordinately regulated by the circadian clock and Wnt signaling in the intestine.

Given the importance of the intestinal clock in regulating MDSCs, we now provide evidence that MDSC accumulation is time-of-day regulated (Figure 5A–D). Importantly, our data illustrate that MDSCs peak in abundance at the beginning of the active phase, suggesting a temporal window of heightened immunosuppression. Previous studies have also shown that environmental clock disruption paradigms remodel the immune cell landscape including enhanced recruitment of macrophages and regulatory T cells[27,68]. Our findings now expand the repertoire of anti-tumor immunity to include clock-dependent control of immunosuppression through MDSCs. Based on this data, we leveraged this rhythmic control of immunosuppressive cells to show that timing of anti-PD-L1 delivery impacts treatment efficacy and outcome in models of CRC, lung cancer, and melanoma (Figure 5).

Finally, immunotherapy is not effective in all tumor types[129–132], and of ICI-responsive cancers, many patients subsequently demonstrate disease progression[14,15]. Circadian medicine approaches, including chronotherapy, suggest that timing of certain chemotherapies could provide therapeutic advantage when dosed at the optimal time of day[29–31,133–135]. We now provide evidence that immunotherapy follows a similar rationale based on the molecular underpinnings of clock-dependent control of immunosuppressive MDSCs within the tumor microenvironment. Moreover, retrospective analysis of clinical data suggest that dosing of ICIs during the early active phase could provide therapeutic benefit in multiple tumor types[38–41]. These clinical studies are in line with our findings and further support the need for prospective clinical trials investigating the time-of-day dependent efficacy of immune checkpoint therapies in the treatment of solid tumors.

Methods:

Mice

Apc mice that harbor a heterozygous floxed allele of exons 1 to 15 (*Apc*$^{+/\ ex1-15}$)[56] were crossed with *Bmal1* conditional mice that carry homozygous floxed alleles of exon 8 (*Bmal1*$^{fl/fl}$)[136]. Intestine-specific targeting of epithelial cells was achieved by crossing these conditional mice with Villin-Cre animals to create *Apc*$^{+/\ ex1-15}$;*Bmal1*$^{fl/fl}$;*Villin-Cre* mice. All mouse strains are on a C57BL/6 background and both males and females aged 9–10 months were used for experiments. Mice were purchased from the Jackson Laboratory (Bar Harbor, ME). All experiments were performed in accordance with the Institutional Animal Care and Use Committee (IACUC) guidelines at the University of California, Irvine. Animals were housed on a standard 12-hour light/12-hour dark paradigm, with temperatures of 65–75 °F, humidity 40–60%, and fed *ad libitum*. The environmental shift disruption (SD) paradigm was performed on 2-month-old WT mice purchased from the Jackson Laboratory (Bar Harbor, ME). Mice were shifted for 1–8 weeks by advancing the light phase by 8 hours every other day. For the circadian ZT 4 and ZT 16 experiments, WT and *Apc*$^{+/-}$;*Bmal1*$^{-/-}$ mice were divided into two groups. One group was kept in normal 12 hour light:12 hour dark conditions (LD), and the other group was kept in an inverted 12 hour dark:12 hour light condition (DL) in order to perform flow cytometry at the same time.

Spleen tissue collection and cell isolation

Animals were sacrificed at the ZT indicated in the legend, spleens were quickly excised, pushed through a 70-μm cell strainer to create a cell suspension of splenocytes and washed with RPMI. Cells were centrifuged at 500g at 4°C for 10 min and then incubated for 1 min in 5 mL RBC lysis buffer at RT. Cells were quenched with 10 mL serum-free PBS and pelleted by centrifugation at 500g at 4°C for 5 min. Cells were resuspended in 5 mL FACS buffer (1xPBS, 10% FBS), and total remaining live cells were counted by Countess™ II and processed for downstream FACS analysis.

Small intestine tissue collection and cell isolation

Tissue samples were harvested from mice at the ZT indicated in the legend, flushed, and cut longitudinally. Tissues were placed in RPMI media containing 1% FBS, 18 μg/mL DNase1 (Sigma-Aldrich, 04536282001) and 0.6 mg/mL Collagenase type P (Roche, #11249002001) and were digested at 37°C on a shaker for 30 min. Cells were filtered through a 70-μm cell strainer, washed with PBS containing 1M HEPES and 2% FBS. Samples were centrifuged to pellet cells, which were then resuspended in RPMI medium, filtered through a 40-μm cell strainer, and washed with PBS containing 1M HEPES and 2% FBS. Cells were centrifuged at 500g at 4°C for 5 min and then incubated for 1 min in 1 mL RBC lysis buffer at RT. Cells were quenched with 10 mL serum-free PBS and centrifuged at 500g at 4°C for 5 min. Cells were resuspended in 5 mL FACS buffer (1xPBS, 10% FBS), and total remaining live cells were counted by Countess™ II and processed for FACS analysis.

Lymph node collection and cell isolation

The mesenteric, dLN was collected at the ZT indicated in the legend and teased open with a 23G needle before being placed in digestion solution containing 1 mg/mL Collagenase D and A. After incubating at 37 °C on a shaker for 20 min, cells were filtered through a 70-μm cell strainer and washed with PBS. Samples were centrifuged to pellet cells, which were then resuspended in 1 mL FACS buffer (1xPBS, 10% FBS), and total remaining live cells were counted by Countess™ II and processed for FACS analysis.

Bone marrow collection and cell isolation

The femur and tibia were collected and flushed with HBSS supplemented with 2% FBS and 1mM EDTA using a 25G needle. Cells were centrifuged at 500g at 4°C for 5 min, washed with 5 mL HBSS supplemented with 2% FBS and 1mM EDTA, and filtered through a 70-μm cell strainer, and total remaining live cells were counted by Countess™ II.

Blood collection and cell isolation

Blood was collected at the ZT indicated in the legend by cardiac puncture and 0.5M EDTA was added to blood at a ratio of 1:10. Blood was incubated for 5 min in 2 mL RBC lysis buffer at RT. Cells were quenched with 10 mL serum-free PBS and centrifuged at 500g at 4°C for 5 min. Red blood cell lysis was repeated again and then cells were resuspended in 1 mL FACS buffer (1xPBS, 10% FBS), and total remaining live cells were counted by Countess™ II and processed for FACS analysis.

Fluorescence-Activated Cell Sorting (FACS)

Tissue samples were harvested from mice at the ZT indicated in the legend and mechanically dissociated to generate single cell suspensions as described above. Cells were blocked with anti-mouse FcγR (CD16/CD32) (BioLegend, 101301) on ice for 5 min. Cells were then centrifuged at 400g for 3 min at 4°C and washed once with FACS buffer (1xPBS with 10%FBS). Cells were incubated for 30 min at 4°C with pre-conjugated fluorescent labeled antibodies with the following combinations: CD45 [BioLegend, 103112 (APC)], CD11b [BioLegend, 101228 (PerCP/cyanine5.5), 101205 (FITC) or 101225 (APC/Cy7)], Gr1 [BioLegend, 108439 (BV605) or 108407 (PE)], F4/80 [Biolegend, 123110 (PE)], Ly6C [BioLegend, 128035 (BV605)], Ly6G [BioLegend, 127606 (FITC)], CD3 [TONBO Biosciences, 50–0032 (PE)], CD4 [Life Technologies, 46-0042-82 (eFluor710)], CD8 [RndSystems, FAB116G (AlexaFluor488)], CD25 [BioLegend, 102037 (BV650)], and PD-L1 [Tonbo Biosciences, 50–1243 (PE)]. Sytox Blue dye (Life Technologies, S34857) was added to stained cells to assay for viability. Cells were sorted by BD FACSAria™ Fusion and desired populations were isolated for downstream experiments. Data was analyzed using FlowJo software, v10.0.7 (Tree Star, Inc).

T cell Suppression Assay

Spleens were dissected, filtered into a single-cell suspension and depleted of red blood cells using Tris-acetic-acid-chloride (TAC). T cells were isolated from the spleen using the EasySep™ Mouse T cell Isolation Kit (StemCell Technologies, 19851) according to the manufacturer's instructions. Isolated T cells were washed once with PBS and resuspended at

15×10^6/mL in staining buffer (0.01% BSA in PBS). T cells were stained with proliferation dye eFluor™ 670 (ThermoFisher Scientific, 65-0840-85) using 5mM dye per 1×10^7 cells and incubated in a 37°C water bath for 10 min. Finally, T cells were washed and resuspended at 1×10^6/mL in RPMI 1640 w/ HEPES+ L-glutamine complete medium containing 10% FBS, 1X non-essential amino acids, 100U/mL penicillin-100μg/mL streptomycin, 1mM sodium pyruvate, and 55 μM β-mercaptoethanol. eFluor™ 670-labeled T cells were plated (50×10^3/well) in a U-bottom 96-well plate and activated with plate bound anti-Armenian hamster IgG (30μg/mL, Jackson ImmunoResearch, 127-005-099), with CD3 (0.5 μg/mL, Tonbo, 70–0031) and CD28 (1 μg/mL, Tonbo, 70–0281). Sorted CD11b$^+$ Gr1$^+$ cells were added to T cells in 1:1 ratio (50×10^3 T cells:50×10^3 CD11b$^+$ Gr1$^+$ cells). After 3 days of culture, cells were collected and blocked with anti-mouse CD16/32 (BioLegend, 101302), stained with Zombie Live/Dead Dye (BioLegend, 423105) and fluorescent-conjugated antibodies: CD4 (BioLegend, 100512; clone RM4–5) and CD8 (BioLegend, 100709; clone 53–6.7). Single-stained samples and fluorescence minus one (FMO) controls were used to establish PMT voltages, gating, and compensation parameters. Cells were processed using the BD LSR II or BD LSRFortessa™ X-20 flow cytometer and analyzed using FlowJo software, v10.0.7 (Tree Star, Inc).

ROS Production Assay

Cells were harvested from respective tissues and processed to single cell suspensions as described above. Cells were stained with CD45, CD11b, and Gr1 antibodies as described above. Following staining, cells were resuspended in FACS buffer and 10mM 2′,7′-Dichlorofluorescein diacetate (H$_2$DCFDA) (Sigma-Aldrich, D6883) was added and incubated for 30 min at RT. Cells were then processed on the BD FACSAria™ Fusion and analyzed using FlowJo software, v10.0.7 (Tree Star, Inc).

Cytokine/chemokine ELISA

WT and *Bmal1*$^{-/-}$ primary intestinal monolayers were cultured with or without 100 ng/mL recombinant mouse Wnt3a (Peprotech, 315–20). Undiluted CM and cell lysate were profiled using the 32-plex Discovery Assay (Mouse Cytokine/Chemokine 32-Plex Panel, Eve Technologies, Alberta, Canada).

Primary Neutrophil Assays

Neutrophils were isolated from mouse bone marrow using the EasySep Mouse Neutrophil Enrichment Kit (STEMCELL Technologies, 19762). For the migration assay, 1 million neutrophils were plated in the top well of a 24 well transwell insert (Corning, 3378) and WT or *Bmal1*$^{-/-}$ intestinal monolayer CM was added to the bottom well. After 18 hours, neutrophils that migrated to the bottom well were counted. For the culture with intestinal monolayer CM, 500,000 neutrophils were plated in a 24 well plate with intestinal monolayer CM. After 24 hours, neutrophils were collected for RNA isolation and qPCR analysis.

Mouse intestinal organoid isolation and culturing

The following protocol for isolation and culture of mouse intestinal organoids was used with minor modifications, based on previously published methods[137]. The intestinal segment

was dissected into small pieces and incubated in dissociation solution (PBS supplemented with 2 mM EDTA and 10 μM Rho kinase inhibitor Y-27632) for 1 hour at 4°C with agitation. Next, intestinal tissue pieces were shaken, strained, and centrifuged. Pellets were resuspended in Matrigel (Corning Inc.) and ENR medium was added. ENR is a basal medium supplemented with recombinant murine EGF (50 ng/ml) (PeproTech), recombinant murine Noggin (50 ng/ml) (PeproTech), 1 mM N-acetylcysteine (Sigma-Aldrich), and 20% (v/v) of R-Spondin CM (*Rspo1*-expressing cells, Trevigen). The basal medium is advanced Dulbecco's modified Eagle's medium (DMEM)/F12 (Gibco) supplemented with 3 mM L-glutamine (Thermo Fisher Scientific), Primocin (100 μg/ml) (InvivoGen), and 10 mM Hepes (Sigma-Aldrich). For primary intestinal epithelial monolayer culture, dissociated intestinal tissues were centrifuged and resuspended in ENR medium supplemented with Y-27632 (Biogems) and 10 μM CHIR-99021 (Sigma-Aldrich), and then seeded on top of a Matrigel-coated cell culture plate.

Western blot

Organoid pellets were lysed in radioimmunoprecipitation assay lysis buffer [50 mM tris (pH 8), 150 mM NaCl, 5 mM EDTA, 15 mM $MgCl_2$, and 1% NP-40] containing protease and phosphatase inhibitors [1× complete EDTA free cocktail tablet (Sigma-Aldrich), 0.5 mM phenylmethylsulfonyl fluoride, 20 mM NaF, 1 mM Na_3VO_4, 1 μM trichostatin A, and 10 mM nicotinamide]. Protein lysates were resolved on an SDS–polyacrylamide gel. Antibodies used for Western blot were the following: c-MYC (Abcam, ab32072) and p84 (GeneTex, GTX70220).

Lentiviral transduction of organoids

The third-generation lentiviral packaging system was used for transduction of intestinal organoids. For production of viral particles, HEK293T cells were transfected with plasmids encoding lentiviral packaging (pRSV-Rev and pMDLg/pRRE), lentiviral envelope (pMD2.G), and the desired transfer vector. Lentivirus-containing medium was harvested 48 hours after transfection, filtered through a 0.45-μm syringe filter, and concentrated over 100-fold in volume by ultracentrifugation. For transduction of organoid monolayers, virus was incubated with 10 μg/mL polybrene in medium supplemented with Y-27632 (Biogems) and 10 μM CHIR-99021 (Sigma-Aldrich). Primary intestinal monolayers were collected 48 hours later. For the lentiviral transduction of *c-Myc* shRNA in WT intestinal monolayers, Lenti-sh1368 plasmid was used (Addgene, #29435).

Single-Cell RNA Sequencing (scRNAseq)

FACS-sorted CD45^{+} cells were isolated at ZT 4 from the small intestine of 9–10 month old WT, *Bmal1*^{−/−}, *Apc*^{+/−} and *Apc*^{+/−};*Bmal1*^{−/−} mice (n=3 mice/genotype). Cells were washed once in PBS with 0.04% BSA, and a total of $0.2–2×10^6$ cells per genotype were used for cell multiplexing barcoding using the CellPlex Kit (10X Genomics), according to manufacturer's instructions. Briefly, cells were pelleted after washing by centrifugating at 300 rcf, for 5 minutes at room temperature, and resuspended in 100 μl Cell Multiplexing Oligos (one oligo/barcode per genotype). Oligos were allowed to bind cell membranes by incubating at room temperature for 5 min, and unbound multiplexing oligos were washed 3 times with 2 ml ice-cold PBS + 1% BSA. After washing, cells were resuspended in

chilled PBS + 1% BSA to a concentration of approximately 1,000 cell/μL, and loaded onto the 10X Genomics Chromium Controller for droplet-enabled scRNAseq according to the manufacturer's instructions. Library generation was performed following the Chromium NextGEM Single Cell v3.1 Cell Multiplexing Reagents Kits User Guide: CG000388Rev B. A total of 3 libraries were generated, each of them consisting of a pool of equal cell numbers from CD45+ cells from the small intestine of each genotype. Multiplexed, single cell gene expression libraries were sequenced on the Illumina HiSeq. Alignment of 3' end counting libraries from scRNAseq analyses was completed utilizing 10× Genomics CellRanger-6.1.2. Each library was aligned to an indexed mm10 genome using cellranger count.

Mouse scRNA-seq data analysis

All scRNA-seq analysis was performed in R (v4.2.1) using Rstudio (v 2023.03.1 Build 446) and the Seurat v4 package[138]. Cell Ranger outputs were loaded into R using the Read10X() function, and Seurat objects from each sample were generated using the CreateSeuratObject() function, where genes that were not detected in at least 3 cells (min.cells = 3) and cells containing less than 200 different genes (min.features = 200) were excluded. Seurat objects containing single cell gene expression data from each sample were merged using the merge() function, and percentages of mitochondrial genes (percent.mt) expressed in each cell were calculated using the PercentageFeatureSet() function. Low quality cells were filtered out from Seurat objects utilizing the subset() function, where only cells with nFeature_RNA > 200 and < 8,000, and percent.mt < 20 were carried forward in the analysis. After removing low quality cells, Seurat objects were normalized using the NormalizeData() function, using the "LogNormalize" method and a scale factor of 10,000. After normalization, the top 2,000 most variable genes were calculated using the FindVariableFeatures() function, utilizing the vst selection method. Data was then scaled for dimensionality reduction using the ScaleData() function, and linear dimensionality reduction was calculated with the RunPCA() function using the variable features. Then, the FindNeighbors() function and the RunUMAP() functions were run using 20 PCs. Clustering was achieved using the FindClusters() function, and cluster identities were manually assigned after examining top expressed genes in each cluster using the FindAllMarkers() function. The function FindAllMarkers() performs differential gene expression between two groups using the Wilcoxon Rank Sum test by default, which are then plotted in the heat maps produced with DoHeatmap() where the selected number of top genes per cell cluster are shown. This function only returns genes that have a p-value below the specified threshold (default = 0.01). This provided data for 17,692 cells. The data was analyzed again for low quality cells; this time, cells with nFeature < 3,000 and percent.mt < 10 were additionally excluded. This step reduced the data to 15,234 cells. For T cell and myeloid subclustering, the data were subset by appropriate cell types: "neutrophils" and "monocytes/ macrophages/dendritic cells" for the myeloid subclustering and "CD4 T cells", "CD8 T cells", and "double negative (DN) T cells" for the T cell subclustering. Then, normalization, scaling, and immune cell marker analysis were performed again. To additionally analyze cell types highly expressing PD-L1 (CD274), subsetting was performed with cells having PD-L1 expression > 2.

RNA extraction and gene expression analysis

Total RNA from sorted single cells was extracted using a Direct-zol RNA microprep kit (Zymo Research). To generate cDNA, equal amounts of total RNA were incubated with Maxima H Minus cDNA Synthesis Master Mix (Thermo Fisher Scientific) according to the manufacturer's instructions. cDNA was used for quantitative real-time PCR using PowerUp SYBR Green Master Mix (Applied Biosystems). Gene expression was normalized to 18S ribosomal RNA. Primer sequences used for gene expression analysis by qPCR are listed in Table 1.

Human scRNA-seq data analysis

All human scRNA-seq analysis was performed in R (v4.2.1) using Rstudio (v 2023.03.1 Build 446) and the Seurat v4 package[138]. Data was obtained from Pelka et al.[117], downloaded, and converted into a Seurat object. Percentages of mitochondrial genes (percent.mt) expressed in each cell were calculated using the PercentageFeatureSet() function. The data had been prefiltered by Pelka et al. to percent.mt < 50, and this was determined as the optimal threshold. Low quality cells were filtered out from Seurat objects utilizing the subset() function, where only cells with nFeature_RNA > 200 and < 8,000, and nCount_RNA < 10,000 were carried forward in the analysis. After removing low quality cells, the Seurat object was additionally subset to cells expressing CD45 (PTPRC) > 0.5 in order to focus on immune cells, resulting in 82,611 cells. The object was then normalized using the NormalizeData() function, using the "LogNormalize" method and a scale factor of 10,000. After normalization, the top 5,000 most variable genes were calculated using the FindVariableFeatures() function, utilizing the vst selection method. Data was then scaled for dimensionality reduction using the ScaleData() function, and linear dimensionality reduction was calculated with the RunPCA() function using the variable features. Then, the FindNeighbors() and the RunUMAP() functions were run using 20 PCs. Clustering was achieved using the FindClusters() function with a resolution of 0.8, and cluster identities were manually assigned after examining the expression of immune-lineage specific genes in each cluster using the DotPlot() function (Figure S9A). The function FindAllMarkers() performs differential gene expression between two groups using the Wilcoxon Rank Sum test by default, which are then plotted in the heat maps produced with DoHeatmap() where the selected number of top genes per cell cluster are shown. This function only returns genes that have a p-value below the specified threshold (default = 0.01). To appropriately compare normal and tumor tissue, final analyses were reported after subsetting to only immune cell data from patients with matched tumor and normal tissue samples, resulting in 55,535 cells from 36 patients. Expression of PD-L1 (CD274) was additionally analyzed by subsetting the object to cells with PD-L1 expression > 0, resulting in 1,253 cells.

Anti-PD-L1 treatment in *Apc*^{+/−};*Bmal1*^{−/−} mice

Apc^{+/−};*Bmal1*^{−/−} mice were randomized into two groups, ZT 4 and ZT 16. For injections to be performed at the same time of day, ZT 16 mice were put in a separate room with inverted light schedule. Mice were subjected to a gradual shift in time (1 hour/day) to minimize systemic circadian disruption. Anti-PD-L1 (BioLegend, 124329) was administered

two times weekly (200 µg per mouse) by intraperitoneal injection. After 3 weeks, mice were sacrificed for tumor burden and flow cytometric analysis.

Anti-PD-L1 treatment in subcutaneous models

Mice received a subcutaneous injection of 1×10^6 MC38 cells, 2×10^6 D4M-S cells, or 2×10^6 CMT167 cells per tumor at ZT 4. Cells were resuspended in Matrigel to facilitate engraftment. Two tumors were injected per mouse 1cm off the midline in both sides of the abdomen. IgG (BioLegend, 400668) or anti-PD-L1 (BioLegend, 124329) were administered every 2–3 days (200 µg per mouse) for a total of 4 treatments by intraperitoneal injection. Mice were sacrificed before the tumor size exceeded 1000 mm^3.

Statistical Analysis

Sample sizes were determined using the proper power analysis test for either t-test or one-way ANOVA and a confidence of 90%. Data distribution was assumed to be normal but this was not formally tested. Statistical analyses were performed in Prism 10 (GraphPad Software). Visualization was performed using Prism 10 (GraphPad Software), Seurat, or ggplot2(). All resulting graphs are shown as mean ± SEM with details of the statistical test used specified in the legend. Animals were randomized prior to beginning experiments and data collection and analyses were not performed blind.

Supplementary Material

Refer to Web version on PubMed Central for supplementary material.

Acknowledgements:

Data availability:

The single cell RNA-sequencing data have been deposited at the NCBI Gene Expression Omnibus (GEO) under the GEO accession number GSE262267 and at the Sequence Read Archive (SRA) under SRA accession number PRJNA1003452.

References:

1. Bailey CE et al. Increasing disparities in the age-related incidences of colon and rectal cancers in the United States, 1975–2010. JAMA Surgery 150, 17–22 (2015). [PubMed: 25372703]

2. Ben-Aharon I et al. Early-Onset Cancer in the Gastrointestinal Tract Is on the Rise—Evidence and Implications. Cancer Discovery 13, 538–551 (2023). [PubMed: 36757194]

3. Sinicrope FA Increasing Incidence of Early-Onset Colorectal Cancer. New England Journal of Medicine 386, 1547–1558 (2022). [PubMed: 35443109]

4. Siegel RL, Miller KD, Wagle NS & Jemal A Cancer statistics, 2023. CA: A Cancer Journal for Clinicians 73, 17–48 (2023). [PubMed: 36633525]

5. Tsalic M, Bar-Sela G, Beny A, Visel B & Haim N Severe Toxicity Related to the 5-Fluorouracil/ Leucovorin Combination (The Mayo Clinic Regimen): A Prospective Study in Colorectal Cancer Patients. American Journal of Clinical Oncology 26, 103 (2003). [PubMed: 12576935]

6. Meulendijks D et al. Clinical relevance of DPYD variants c.1679T>G, c.1236G>A/HapB3, and c.1601G>A as predictors of severe fluoropyrimidine-associated toxicity: a systematic review and meta-analysis of individual patient data. The Lancet Oncology 16, 1639–1650 (2015). [PubMed: 26603945]

7. Meulendijks D et al. Pretreatment serum uracil concentration as a predictor of severe and fatal fluoropyrimidine-associated toxicity. Br J Cancer 116, 1415–1424 (2017). [PubMed: 28427087]

8. Mikhail SE, Sun JF & Marshall JL Full article: Safety of capecitabine: a review. https:// www.tandfonline.com/doi/full/10.1517/14740338.2010.511610.

9. Xie Y-H, Chen Y-X & Fang J-Y Comprehensive review of targeted therapy for colorectal cancer. Sig Transduct Target Ther 5, 1–30 (2020).

10. Sharma P & Allison JP The future of immune checkpoint therapy. Science 348, 56–61 (2015). [PubMed: 25838373]

11. Darvin P, Toor SM, Sasidharan Nair V & Elkord E Immune checkpoint inhibitors: recent progress and potential biomarkers. Exp Mol Med 50, 1–11 (2018).

12. Diaz LA et al. Pembrolizumab versus chemotherapy for microsatellite instability-high or mismatch repair-deficient metastatic colorectal cancer (KEYNOTE-177): final analysis of a randomised, open-label, phase 3 study. The Lancet Oncology 23, 659–670 (2022). [PubMed: 35427471]

13. André T et al. Pembrolizumab in Microsatellite-Instability–High Advanced Colorectal Cancer. New England Journal of Medicine 383, 2207–2218 (2020). [PubMed: 33264544]

14. Antonia SJ et al. Four-year survival with nivolumab in patients with previously treated advanced non-small-cell lung cancer: a pooled analysis. Lancet Oncol 20, 1395–1408 (2019). [PubMed: 31422028]

15. Larkin J et al. Five-Year Survival with Combined Nivolumab and Ipilimumab in Advanced Melanoma | NEJM. (2019).

16. Takahashi JS Transcriptional architecture of the mammalian circadian clock. Nature Reviews Genetics 18, 164–179 (2017).

17. Bass J & Lazar MA Circadian time signatures of fitness and disease | Science. https://www.science.org/doi/10.1126/science.aah4965? url_ver=Z39.88-2003&rfr_id=ori:rid:crossref.org&rfr_dat=cr_pub%20%200pubmed.

18. Pariollaud M & Lamia KA Cancer in the Fourth Dimension: What is the impact of circadian disruption? Cancer Discov 10, 1455–1464 (2020). [PubMed: 32934020]

19. Scheiermann C, Gibbs J, Ince L & Loudon A Clocking in to immunity. Nat Rev Immunol 18, 423–437 (2018). [PubMed: 29662121]

20. Benitah SA & Welz P-S Circadian Regulation of Adult Stem Cell Homeostasis and Aging. Cell Stem Cell 26, 817–831 (2020). [PubMed: 32502402]

21. Gibbs J et al. An epithelial circadian clock controls pulmonary inflammation and glucocorticoid action. Nature Medicine 20, 919–926 (2014).

22. Méndez-Ferrer S, Lucas D, Battista M & Frenette PS Haematopoietic stem cell release is regulated by circadian oscillations. Nature 452, 442–447 (2008). [PubMed: 18256599]

23. Curtis AM, Bellet MM, Sassone-Corsi P & O'Neill LAJ Circadian Clock Proteins and Immunity. Immunity 40, 178–186 (2014). [PubMed: 24560196]

24. Gibbs J et al. The nuclear receptor REV-ERBα mediates circadian regulation of innate immunity through selective regulation of inflammatory cytokines. Proceedings of the National Academy of Sciences of the United States of America 109, 582–7 (2012). [PubMed: 22184247]

25. Sutton CE et al. Loss of the molecular clock in myeloid cells exacerbates T cell-mediated CNS autoimmune disease. Nat Commun 8, 1923 (2017). [PubMed: 29234010]

26. Nguyen KD et al. Circadian gene Bmal1 regulates diurnal oscillations of Ly6C(hi) inflammatory monocytes. Science (New York, N.Y.) 341, 1483–8 (2013). [PubMed: 23970558]

27. Hadadi E et al. Chronic circadian disruption modulates breast cancer stemness and immune microenvironment to drive metastasis in mice. Nature Communications 11, (2020).

28. Wang C et al. Dendritic cells direct circadian anti-tumor immune responses. Nature 1–3 (2022) doi: 10.1038/s41586-022-05605-0.

29. Lévi F, Zidani R & Misset JL Randomised multicentre trial of chronotherapy with oxaliplatin, fluorouracil, and folinic acid in metastatic colorectal cancer. International Organization for Cancer Chronotherapy. Lancet 350, 681–686 (1997). [PubMed: 9291901]

30. Levi FA et al. Chronomodulated Versus Fixed-Infusion-Rate Delivery of Ambulatory Chemotherapy With Oxaliplatin, Fluorouracil, and Folinic Acid (Leucovorin) in Patients With Colorectal Cancer Metastases: A Randomized Multi-Institutional Trial. https://academic.oup.com/jnci/article/86/21/1608/1062103 (1994).

31. Gou XX et al. Induction chronomodulated chemotherapy plus radiotherapy for nasopharyngeal carcinoma: A Phase II prospective randomized study. Journal of Cancer Research and Therapeutics 14, 1613–1619 (2018). [PubMed: 30589048]

32. Kemeny MM, Alava G & Oliver JM Improving responses in hepatomas with circadian-patterned hepatic artery infusions of recombinant interleukin-2. J Immunother (1991) 12, 219–223 (1992). [PubMed: 1477073]

33. Koren S, Whorton EB Jr. & Fleischmann WR Jr. Circadian Dependence of Interferon Antitumor Activity in Mice. JNCI: Journal of the National Cancer Institute 85, 1927–1932 (1993). [PubMed: 8230283]

34. Ohdo S, Koyanagi S, Suyama H, Higuchi S & Aramaki H Changing the dosing schedule minimizes the disruptive effects of interferon on clock function. Nat Med 7, 356–360 (2001). [PubMed: 11231636]

35. Iacobelli S et al. A phase I study of recombinant interferon-alpha administered as a seven-day continuous venous infusion at circadian-rhythm modulated rate in patients with cancer. Am J Clin Oncol 18, 27–31 (1995). [PubMed: 7847255]

36. Deprés-Brummer P et al. A phase I trial of 21-day continuous venous infusion of alpha-interferon at circadian rhythm modulated rate in cancer patients. J Immunother (1991) 10, 440–447 (1991). [PubMed: 1768678]

37. Re GL et al. Interleukin-2 chronotherapy for metastatic renal cell carcinoma: Results of a phase I-II study. Cytokine 128, 154984 (2020). [PubMed: 31972343]

38. Qian DC et al. Effect of immunotherapy time-of-day infusion on overall survival among patients with advanced melanoma in the USA (MEMOIR): a propensity score-matched analysis of a single-centre, longitudinal study. The Lancet Oncology 22, 1777–1786 (2021). [PubMed: 34780711]

39. Landre T et al. Time-dependent efficacy of immune checkpoint inhibitors in the treatment of metastatic cancers: A meta-analysis. in Journal of Clinical Oncology vol. 41 2562–2562 (Wolters Kluwer, 2023).

40. Karaboué A et al. Time-Dependent Efficacy of Checkpoint Inhibitor Nivolumab: Results from a Pilot Study in Patients with Metastatic Non-Small-Cell Lung Cancer. Cancers (Basel) 14, 896 (2022). [PubMed: 35205644]

41. Yeung C, Kartolo A, Tong J, Hopman W & Baetz T Association of circadian timing of initial infusions of immune checkpoint inhibitors with survival in advanced melanoma | Immunotherapy. Immunotherapy (2023).

42. England CG et al. Preclinical Pharmacokinetics and Biodistribution Studies of 89Zr-Labeled Pembrolizumab. Journal of Nuclear Medicine 58, 162–168 (2017). [PubMed: 27493273]

43. Chan AB et al. CRY2 missense mutations suppress P53 and enhance cell growth. Proceedings of the National Academy of Sciences of the United States of America 118, (2021).

44. Papagiannakopoulos T et al. Circadian Rhythm Disruption Promotes Lung Tumorigenesis. Cell metabolism 24, 324–31 (2016). [PubMed: 27476975]

45. Kettner NM et al. Circadian Homeostasis of Liver Metabolism Suppresses Hepatocarcinogenesis. Cancer Cell 30, 909–924 (2016). [PubMed: 27889186]

46. Fekry B et al. Incompatibility of the circadian protein BMAL1 and HNF4α in hepatocellular carcinoma. Nature Communications 9, 4349 (2018).

47. Lee, Donehower LA, Herron AJ, Moore DD & Fu L Disrupting circadian homeostasis of sympathetic signaling promotes tumor development in mice. PLoS ONE 5, (2010).

48. Stokes K et al. The Circadian Clock Gene, Bmal1, Regulates Intestinal Stem Cell Signaling and Represses Tumor Initiation. Cellular and molecular gastroenterology and hepatology 0, (2021).

49. Sulli G et al. Pharmacological activation of REV-ERBs is lethal in cancer and oncogene-induced senescence. Nature 553, 351–355 (2018b). [PubMed: 29320480]

50. Pariollaud M et al. Circadian Disruption Enhances HSF1 Signaling and Tumorigenesis in Kras-Driven Lung Cancer. Sci. Adv vol. 8 1123 https://www.science.org (2022).

51. Fu L, Pelicano H, Liu J, Huang P & Lee CC The Circadian Gene Period2 Plays an Important Role in Tumor Suppression and DNA Damage Response In Vivo. Cell 111, 41–50 (2002). [PubMed: 12372299]

52. Wood PA et al. Period 2 mutation accelerates ApcMin/+ tumorigenesis. Molecular cancer research : MCR 6, 1786–93 (2008). [PubMed: 19010825]

53. Chun SK et al. Disruption of the Circadian Clock Drives Apc Loss of Heterozygosity to Accelerate Colorectal Cancer. Sci. Adv vol. 8 2389 (2022).

54. Dong Z et al. Targeting glioblastoma stem cells through disruption of the circadian clock. Cancer Discovery 9, 1556–1573 (2019). [PubMed: 31455674]

55. Chen P et al. Circadian regulator CLOCK recruits immune-suppressive microglia into the GBM tumor microenvironment. Cancer Discovery 10, 371–381 (2020). [PubMed: 31919052]

56. Cheung AF et al. Complete deletion of Apc results in severe polyposis in mice. Oncogene 29, 1857–64 (2010). [PubMed: 20010873]

57. Keller M et al. A circadian clock in macrophages controls inflammatory immune responses. Proceedings of the National Academy of Sciences of the United States of America (2009).

58. Stewart A et al. Single-Cell Transcriptomic Analyses Define Distinct Peripheral B Cell Subsets and Discrete Development Pathways. Front. Immunol 12, (2021).

59. Daamen AR, Alajoleen RM, Grammer AC, Luo XM & Lipsky PE Single-cell RNA sequencing analysis reveals the heterogeneity of IL-10 producing regulatory B cells in lupus-prone mice. Front Immunol 14, 1282770 (2023). [PubMed: 38155972]

60. Downs-Canner SM, Meier J, Vincent BG & Serody JS B Cell Function in the Tumor Microenvironment. Annual Review of Immunology 40, 169–193 (2022).

61. Wei Y et al. B cell heterogeneity, plasticity, and functional diversity in cancer microenvironments. Oncogene 40, 4737–4745 (2021). [PubMed: 34188249]

62. Laumont CM & Nelson BH B cells in the tumor microenvironment: Multi-faceted organizers, regulators, and effectors of anti-tumor immunity. Cancer Cell 41, 466–489 (2023). [PubMed: 36917951]

63. Liu R-X et al. Altered B cell immunoglobulin signature exhibits potential diagnostic values in human colorectal cancer. iScience 26, 106140 (2023). [PubMed: 36879799]

64. Shalapour S & Karin M The neglected brothers come of age: B cells and cancer. Seminars in Immunology 52, 101479 (2021). [PubMed: 34215491]

65. James SM, Honn KA, Gaddameedhi S & Van Dongen HPA Shift Work: Disrupted Circadian Rhythms and Sleep—Implications for Health and Well-being. Current Sleep Medicine Reports 3, 104–112 (2017). [PubMed: 29057204]

66. Oosterman JE, Wopereis S & Kalsbeek A The Circadian Clock, Shift Work, and Tissue-Specific Insulin Resistance. Endocrinology 161, bqaa180 (2020). [PubMed: 33142318]

67. Lee E & Kim M Light and life at night as circadian rhythm disruptors. Chronobiology in Medicine 1, 95–102 (2019).

68. Aiello I et al. Circadian disruption promotes tumor-immune microenvironment remodeling favoring tumor cell proliferation. Science Advances 6, (2020).

69. Filipski E et al. Circadian disruption accelerates liver carcinogenesis in mice. Mutation Research/Genetic Toxicology and Environmental Mutagenesis 680, 95–105 (2009).

70. Iwamoto A, Kawai M, Furuse M & Yasuo S Effects of chronic jet lag on the central and peripheral circadian clocks in CBA/N mice. Chronobiology International 31, 189–198 (2014). [PubMed: 24147659]

71. Alshetaiwi H et al. Defining the emergence of myeloid-derived suppressor cells in breast cancer using single-cell transcriptomics. Science immunology 5, (2020).

72. Huang B et al. Gr-1+CD115+ immature myeloid suppressor cells mediate the development of tumor-induced T regulatory cells and T-cell anergy in tumor-bearing host. Cancer Res 66, 1123–1131 (2006). [PubMed: 16424049]

73. Yang R et al. CD80 in immune suppression by mouse ovarian carcinoma-associated Gr-1+CD11b+ myeloid cells. Cancer Res 66, 6807–6815 (2006). [PubMed: 16818658]

74. Douglass SM et al. Myeloid-Derived Suppressor Cells Are a Major Source of Wnt5A in the Melanoma Microenvironment and Depend on Wnt5A for Full Suppressive Activity. Cancer Research 81, 658–670 (2021). [PubMed: 33262126]

75. Zhao H et al. Myeloid-derived itaconate suppresses cytotoxic CD8+ T cells and promotes tumour growth. Nat Metab 4, 1660–1673 (2022). [PubMed: 36376563]

76. Jou E et al. An innate IL-25–ILC2–MDSC axis creates a cancer-permissive microenvironment for *Apc* mutation–driven intestinal tumorigenesis. Science Immunology 7, (2022).

77. Sinha P et al. Proinflammatory S100 Proteins Regulate the Accumulation of Myeloid-Derived Suppressor Cells 1. J Immunol vol. 181 4666–4675 http://www.superarray.com/ (2008). [PubMed: 18802069]

78. Roberts NT, MacDonald CR, Mohammadpour H, Antoch MP & Repasky EA Circadian Rhythm Disruption Increases Tumor Growth Rate and Accumulation of Myeloid‐Derived Suppressor Cells. Advanced Biology 2200031 (2022) doi:10.1002/adbi.202200031.

79. Youn J-I, Nagaraj S, Collazo M & Gabrilovich DI Subsets of Myeloid-Derived Suppressor Cells in Tumor Bearing Mice. J Immunol 181, 5791–5802 (2008). [PubMed: 18832739]

80. Yang L, Edwards CM & Mundy GR Gr-1+CD11b+ Myeloid-Derived Suppressor Cells: Formidable Partners in Tumor Metastasis. J Bone Miner Res 25, 1701–1706 (2010). [PubMed: 20572008]

81. Kusmartsev SA, Li Y & Chen S-H Gr-1+ Myeloid Cells Derived from Tumor-Bearing Mice Inhibit Primary T Cell Activation Induced Through CD3/CD28 Costimulation1. The Journal of Immunology 165, 779–785 (2000). [PubMed: 10878351]

82. Bronte V et al. Recommendations for myeloid-derived suppressor cell nomenclature and characterization standards. Nature Communications 7, (2016).

83. Klement JD et al. Tumor PD-L1 engages myeloid PD-1 to suppress type I interferon to impair cytotoxic T lymphocyte recruitment. Cancer Cell 41, 620–636.e9 (2023). [PubMed: 36917954]

84. Noman MZ et al. PD-L1 is a novel direct target of HIF-1α, and its blockade under hypoxia enhanced MDSC-mediated T cell activation. J Exp Med 211, 781–790 (2014). [PubMed: 24778419]

85. Antonios JP et al. Immunosuppressive tumor-infiltrating myeloid cells mediate adaptive immune resistance via a PD-1/PD-L1 mechanism in glioblastoma. Neuro Oncol 19, 796–807 (2017). [PubMed: 28115578]

86. Nusse R & Clevers H Wnt/β-Catenin Signaling, Disease, and Emerging Therapeutic Modalities. Cell 169, 985–999 (2017). [PubMed: 28575679]

87. Casey SC et al. MYC Regulates the Anti-Tumor Immune Response through CD47 and PD-L1. Science 352, 227–231 (2016). [PubMed: 26966191]

88. Li J, Dong T, Wu Z, Zhu D & Gu H The effects of MYC on tumor immunity and immunotherapy. Cell Death Discov. 9, 1–10 (2023). [PubMed: 36588105]

89. Yang C et al. Myc inhibition tips the immune balance to promote antitumor immunity. Cell Mol Immunol 19, 1030–1041 (2022). [PubMed: 35962189]

90. Kortlever RM et al. Myc Cooperates with Ras by Programming Inflammation and Immune Suppression. Cell 171, 1301–1315.e14 (2017). [PubMed: 29195074]

91. Wu X et al. MYC oncogene is associated with suppression of tumor immunity and targeting Myc induces tumor cell immunogenicity for therapeutic whole cell vaccination. J Immunother Cancer 9, e001388 (2021). [PubMed: 33757986]

92. Altay G, Batlle E, Fernández-Majada V & Martinez E In vitro Self-organized Mouse Small Intestinal Epithelial Monolayer Protocol. Bio Protoc 10, e3514 (2020).

93. Kozuka K et al. Development and Characterization of a Human and Mouse Intestinal Epithelial Cell Monolayer Platform. Stem Cell Reports 9, 1976–1990 (2017). [PubMed: 29153987]

94. Moorefield EC, Blue RE, Quinney NL, Gentzsch M & Ding S Generation of renewable mouse intestinal epithelial cell monolayers and organoids for functional analyses. BMC Cell Biology 19, (2018).

95. Liu C et al. Macrophage-derived CCL5 facilitates immune escape of colorectal cancer cells via the p65/STAT3-CSN5-PD-L1 pathway. Cell Death Differ 27, 1765–1781 (2020). [PubMed: 31802034]

96. Wang X et al. Cancer-FOXP3 directly activated CCL5 to recruit FOXP3+Treg cells in pancreatic ductal adenocarcinoma. Oncogene 36, 3048–3058 (2017). [PubMed: 27991933]

97. Coffelt SB et al. IL-17-producing γδ T cells and neutrophils conspire to promote breast cancer metastasis. Nature 522, 345–348 (2015). [PubMed: 25822788]

98. Ajuebor MN, Hogaboam CM, Kunkel SL, Proudfoot AEI & Wallace JL The Chemokine RANTES Is a Crucial Mediator of the Progression from Acute to Chronic Colitis in the Rat1. The Journal of Immunology 166, 552–558 (2001). [PubMed: 11123336]

99. Zhao H et al. Inflammation and tumor progression: signaling pathways and targeted intervention. Sig Transduct Target Ther 6, 1–46 (2021).

100. Zhang Q et al. CCL5-Mediated Th2 Immune Polarization Promotes Metastasis in Luminal Breast Cancer. Cancer Res 75, 4312–4321 (2015). [PubMed: 26249173]

101. Ban Y et al. Targeting Autocrine CCL5-CCR5 Axis Reprograms Immunosuppressive Myeloid Cells and Reinvigorates Antitumor Immunity. Cancer Res 77, 2857–2868 (2017). [PubMed: 28416485]

102. Bie Q et al. IL-17B activated mesenchymal stem cells enhance proliferation and migration of gastric cancer cells. Oncotarget 8, 18914–18923 (2017). [PubMed: 28145881]

103. Shi Y et al. A Novel Cytokine Receptor-Ligand Pair: Identification, Molecular Characterization, and In Vivo Immunomodulatory Activity. Journal of Biological Chemistry 275, 19167–19176 (2000). [PubMed: 10749887]

104. Parsonage G et al. Prolonged, granulocyte–macrophage colony-stimulating factor-dependent, neutrophil survival following rheumatoid synovial fibroblast activation by IL-17 and TNFalpha. Arthritis Res Ther 10, R47 (2008). [PubMed: 18433499]

105. Shen F, Hu Z, Goswami J & Gaffen SL Identification of Common Transcriptional Regulatory Elements in Interleukin-17 Target Genes. Journal of Biological Chemistry 281, 24138–24148 (2006). [PubMed: 16798734]

106. Ernst M & Putoczki T IL-17 Cuts to the Chase in Colon Cancer. Immunity 41, 880–882 (2014). [PubMed: 25526302]

107. Flannigan KL et al. IL-17A-mediated neutrophil recruitment limits expansion of segmented filamentous bacteria. Mucosal Immunol 10, 673–684 (2017). [PubMed: 27624780]

108. Chung AS et al. An interleukin-17–mediated paracrine network promotes tumor resistance to anti-angiogenic therapy. Nat Med 19, 1114–1123 (2013). [PubMed: 23913124]

109. Borish LC & Steinke JW 2. Cytokines and chemokines. Journal of Allergy and Clinical Immunology 111, S460–S475 (2003). [PubMed: 12592293]

110. Kohli K, Pillarisetty VG & Kim TS Key chemokines direct migration of immune cells in solid tumors. Cancer Gene Ther 29, 10–21 (2022). [PubMed: 33603130]

111. Santos I et al. CXCL5-mediated recruitment of neutrophils into the peritoneal cavity of Gdf15-deficient mice protects against abdominal sepsis. Proceedings of the National Academy of Sciences 117, 12281–12287 (2020).

112. Song J, Wu C, Zhang X & Sorokin LM In vivo processing of CXCL5 (LIX) by matrix metalloproteinase (MMP)-2 and MMP-9 promotes early neutrophil recruitment in IL-1β-induced peritonitis. J Immunol 190, 401–410 (2013). [PubMed: 23225890]

113. Metzemaekers M et al. Endogenous modification of the chemoattractant CXCL5 alters receptor usage and enhances its activity toward neutrophils and monocytes. Science Signaling 14, eaax3053 (2021). [PubMed: 33688078]

114. Besnard A-G et al. CXCL6 antibody neutralization prevents lung inflammation and fibrosis in mice in the bleomycin model. Journal of Leukocyte Biology 94, 1317–1323 (2013). [PubMed: 23975892]

115. Gijsbers K et al. GCP-2/CXCL6 synergizes with other endothelial cell-derived chemokines in neutrophil mobilization and is associated with angiogenesis in gastrointestinal tumors. Exp Cell Res 303, 331–342 (2005). [PubMed: 15652347]

116. Li S et al. Interference with glycosaminoglycan-chemokine interactions with a probe to alter leukocyte recruitment and inflammation in vivo. PLoS One 9, e104107 (2014). [PubMed: 25093679]

117. Pelka K et al. Spatially organized multicellular immune hubs in human colorectal cancer. Cell 184, 4734–4752.e20 (2021). [PubMed: 34450029]

118. Zhang B et al. Circulating and Tumor-Infiltrating Myeloid-Derived Suppressor Cells in Patients with Colorectal Carcinoma. PLoS One 8, e57114 (2013). [PubMed: 23437326]

119. Karakasheva TA et al. CD38+ M-MDSC expansion characterizes a subset of advanced colorectal cancer patients. JCI Insight 3, e97022. [PubMed: 29563330]

120. Xiong H et al. Anti–PD-L1 Treatment Results in Functional Remodeling of the Macrophage Compartment. Cancer Research 79, 1493–1506 (2019). [PubMed: 30679180]

121. Beyrend G et al. PD-L1 blockade engages tumor-infiltrating lymphocytes to co-express targetable activating and inhibitory receptors. Journal for ImmunoTherapy of Cancer 7, 217 (2019). [PubMed: 31412943]

122. Deng L et al. Irradiation and anti–PD-L1 treatment synergistically promote antitumor immunity in mice. J Clin Invest 124, 687–695 (2014). [PubMed: 24382348]

123. Huang T et al. Wnt Inhibition Sensitizes PD-L1 Blockade Therapy by Overcoming Bone Marrow-Derived Myofibroblasts-Mediated Immune Resistance in Tumors. Front. Immunol 12, (2021).

124. Juneja VR et al. PD-L1 on tumor cells is sufficient for immune evasion in immunogenic tumors and inhibits CD8 T cell cytotoxicity. Journal of Experimental Medicine 214, 895–904 (2017). [PubMed: 28302645]

125. Pilato MD et al. Targeting the CBM complex causes Treg cells to prime tumors for immune checkpoint therapy. Nature 570, 112–116 (2019). [PubMed: 31092922]

126. Cervantes-Silva MP et al. The circadian clock influences T cell responses to vaccination by regulating dendritic cell antigen processing. Nat Commun 13, 7217 (2022). [PubMed: 36470865]

127. Sato S et al. A circadian clock gene, Rev-erbα, modulates the inflammatory function of macrophages through the negative regulation of Ccl2 expression. J Immunol 192, 407–417 (2014). [PubMed: 24307731]

128. Diamantopoulou Z et al. The metastatic spread of breast cancer accelerates during sleep. Nature 607, 156–162 (2022). [PubMed: 35732738]

129. Ferris RL et al. Durvalumab with or without tremelimumab in patients with recurrent or metastatic head and neck squamous cell carcinoma: EAGLE, a randomized, open-label phase III study. Annals of Oncology 31, 942–950 (2020). [PubMed: 32294530]

130. Zeng N et al. Construction of a Ferroptosis-Related Gene Signature for Predicting Survival and Immune Microenvironment in Melanoma Patients. Int J Gen Med 14, 6423–6438 (2021). [PubMed: 34675611]

131. Garg AD et al. Preclinical efficacy of immune-checkpoint monotherapy does not recapitulate corresponding biomarkers-based clinical predictions in glioblastoma. Oncoimmunology 6, e1295903 (2017). [PubMed: 28507806]

132. Duerinck J et al. Intracerebral administration of CTLA-4 and PD-1 immune checkpoint blocking monoclonal antibodies in patients with recurrent glioblastoma: a phase I clinical trial. J Immunother Cancer 9, e002296 (2021). [PubMed: 34168003]

133. Zhang PX et al. A randomized phase II trial of induction chemotherapy followed by cisplatin chronotherapy versus constant rate delivery combined with radiotherapy. Chronobiology International 35, 240–248 (2018). [PubMed: 29215933]

134. Coudert B et al. A randomized multicenter study of optimal circadian time of vinorelbine combined with chronomodulated 5-fluorouracil in pretreated metastatic breast cancer patients: EORTC trial 05971. Chronobiology International 25, 680–696 (2008). [PubMed: 18780198]

135. Gallion HH et al. Randomized phase III trial of standard timed doxorubicin plus cisplatin versus circadian timed doxorubicin plus cisplatin in stage III and IV or recurrent endometrial carcinoma: A Gynecologic Oncology Group Study. Journal of Clinical Oncology 21, 3808–3813 (2003). [PubMed: 14551299]

136. Storch K-F et al. Intrinsic circadian clock of the mammalian retina: importance for retinal processing of visual information. Cell 130, 730–741 (2007). [PubMed: 17719549]

137. Sato T et al. Single Lgr5 stem cells build crypt-villus structures in vitro without a mesenchymal niche. Nature 459, 262–265 (2009). [PubMed: 19329995]

138. Hao Y et al. Integrated analysis of multimodal single-cell data. Cell 184, 3573–3587.e29 (2021). [PubMed: 34062119]
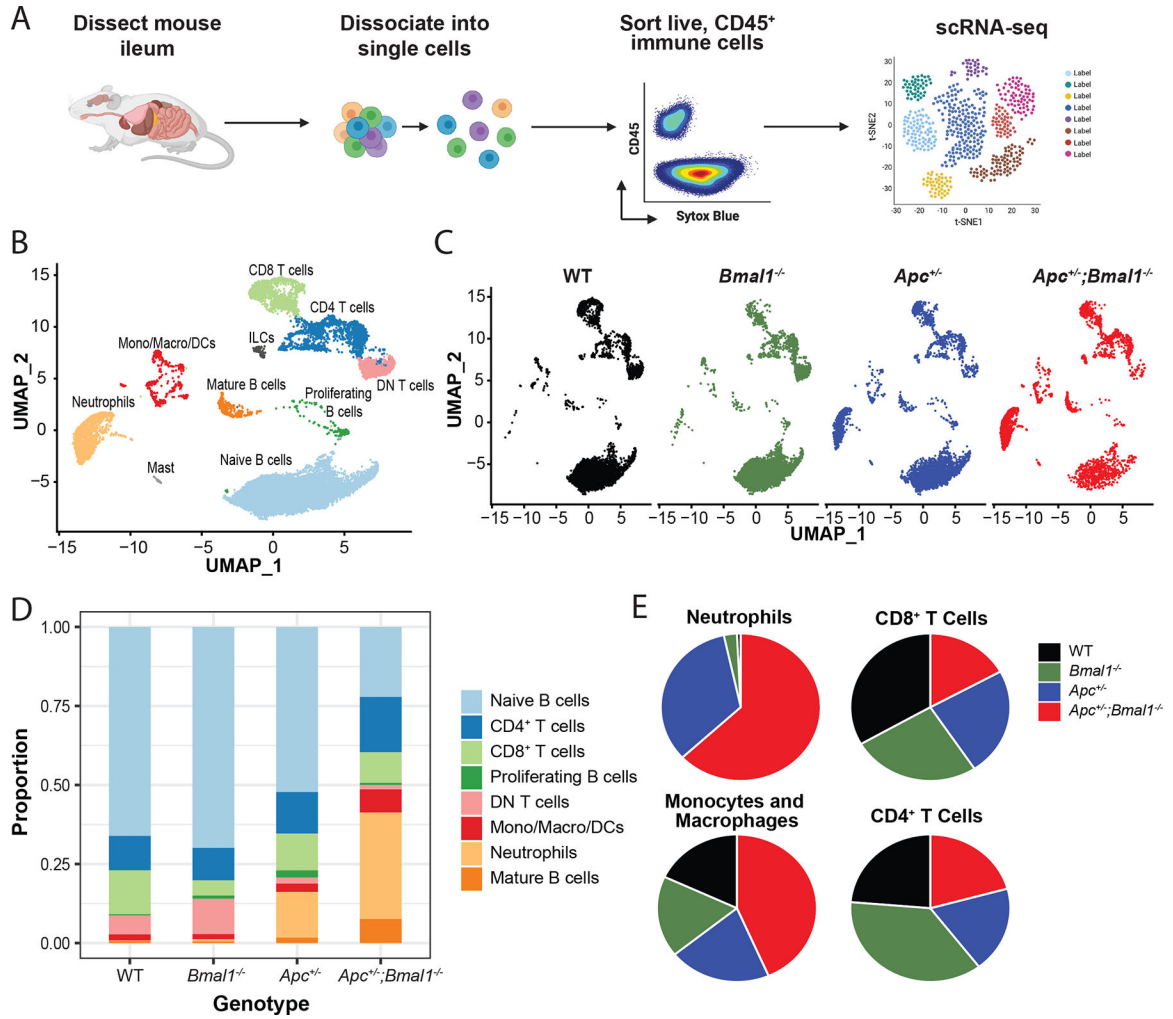
Fig. 1. Circadian clock disruption alters the immune landscape.
(**A**) Schematic depicting the workflow for scRNA-seq of live, CD45^{+} immune cells sorted from mouse small intestine isolated at ZT 4. (**B**) UMAP of cell types clustered by single-cell transcriptional analysis (n=15,234 cells, n= 3 mice/genotype). (**C**) UMAP of cell types clustered by single-cell transcriptional analysis broken down by mouse genotype WT, $Bmal1^{-/-}$, $Apc^{+/-}$, and $Apc^{+/-};Bmal1^{-/-}$. (**D**) Immune cell composition by genotype from WT, $Bmal1^{-/-}$, $Apc^{+/-}$, and $Apc^{+/-};Bmal1^{-/-}$ mice. (**E**) Pie chart of neutrophils, CD8^{+} T cells, monocytes/macrophages, and CD4^{+} T cells from WT, $Bmal1^{-/-}$, $Apc^{+/-}$, and $Apc^{+/-};Bmal1^{-/-}$ mice.
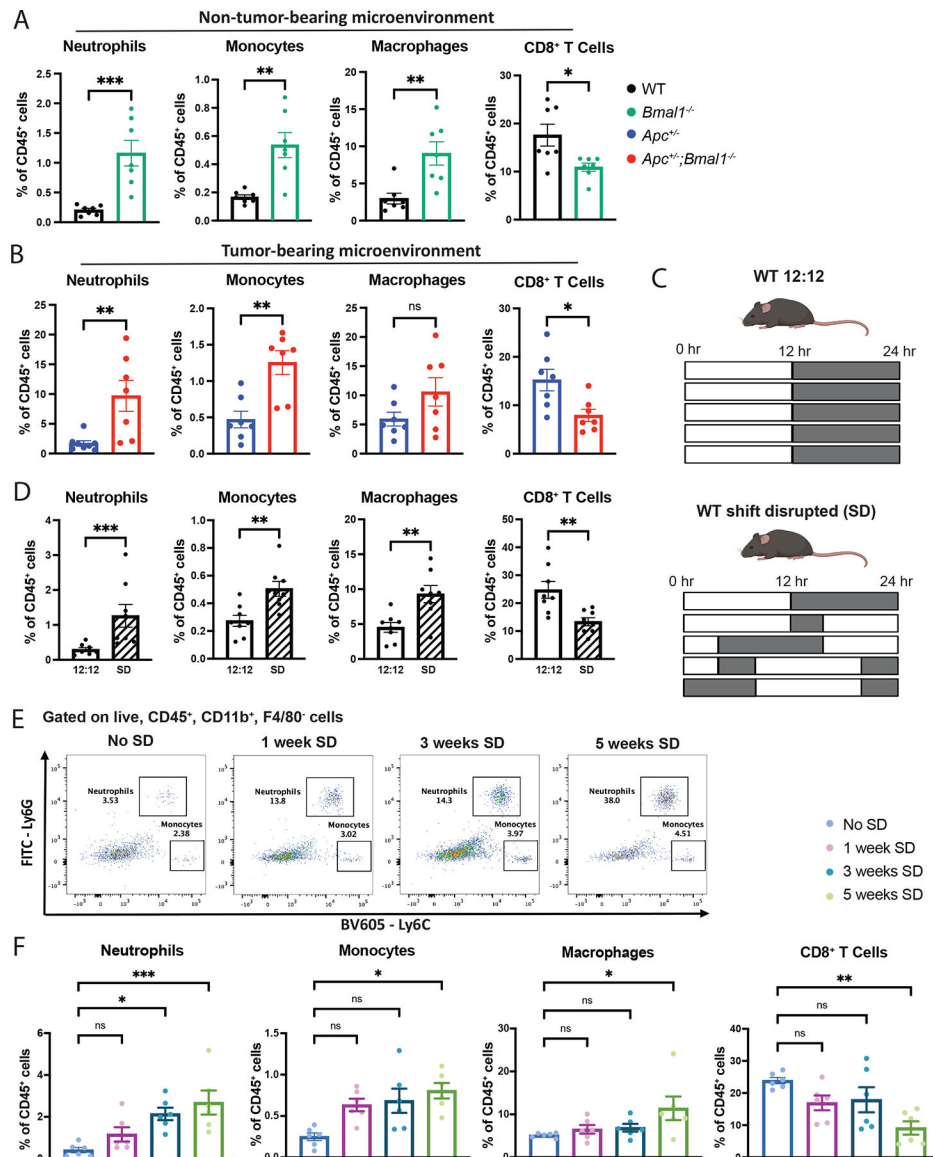
Fig. 2. Genetic and environmental clock disruption alter the immune landscape.
(**A**) Neutrophils, monocytes, macrophages, and CD8+ T cells shown as percent of CD45+ cells from the small intestine of WT and *Bmal1*−/− mice sacrificed at ZT 4 and analyzed by flow cytometry (n=7 mice/genotype). (**B**) Neutrophils, monocytes, macrophages, and CD8+ T cells shown as percent of CD45+ cells from the small intestine of *Apc*+/− and *Apc*+/−;*Bmal1*−/− mice sacrificed at ZT 4 and analyzed by flow cytometry (n=7 mice/genotype). (**C**) Schematic of environmental shift disruption (SD) paradigm in WT mice performed for 8 weeks. Light versus dark schedule is shown for 5 days. (**D**) Neutrophils, monocytes, macrophages, and CD8+ T cells shown as percent of CD45+ cells from the small intestine of WT mice subjected to 12:12 light/dark (LD) versus SD paradigm. Mice were sacrificed at ZT 4 and analyzed by flow cytometry (n=8 mice/genotype). (**E**) Representative proportions of neutrophils and monocytes in the small intestine of WT mice subjected to 12:12 LD paradigm versus 1 week SD, 3 weeks SD, and 5 weeks SD. (**F**) Neutrophils, monocytes,

macrophages, and CD8$^+$ T cells shown as percent of CD45$^+$ cells from the small intestine of WT mice subjected to 12:12 LD paradigm versus 1 week SD, 3 weeks SD, and 5 weeks SD. Mice were sacrificed at ZT 4 and analyzed by flow cytometry (n=6 mice/genotype). Data represent the mean ± SEM and statistical significance was determined by two-tailed Mann-Whitney T-test for A, B, and D, and one-way ANOVA with Tukey's multiple comparison test for F. Asterisks represent p-values from multiple comparisons, with * indicating a p-value of < 0.05, ** indicating a p-value of < 0.01, *** indicating a p-value of < 0.001, and ns = not significant.
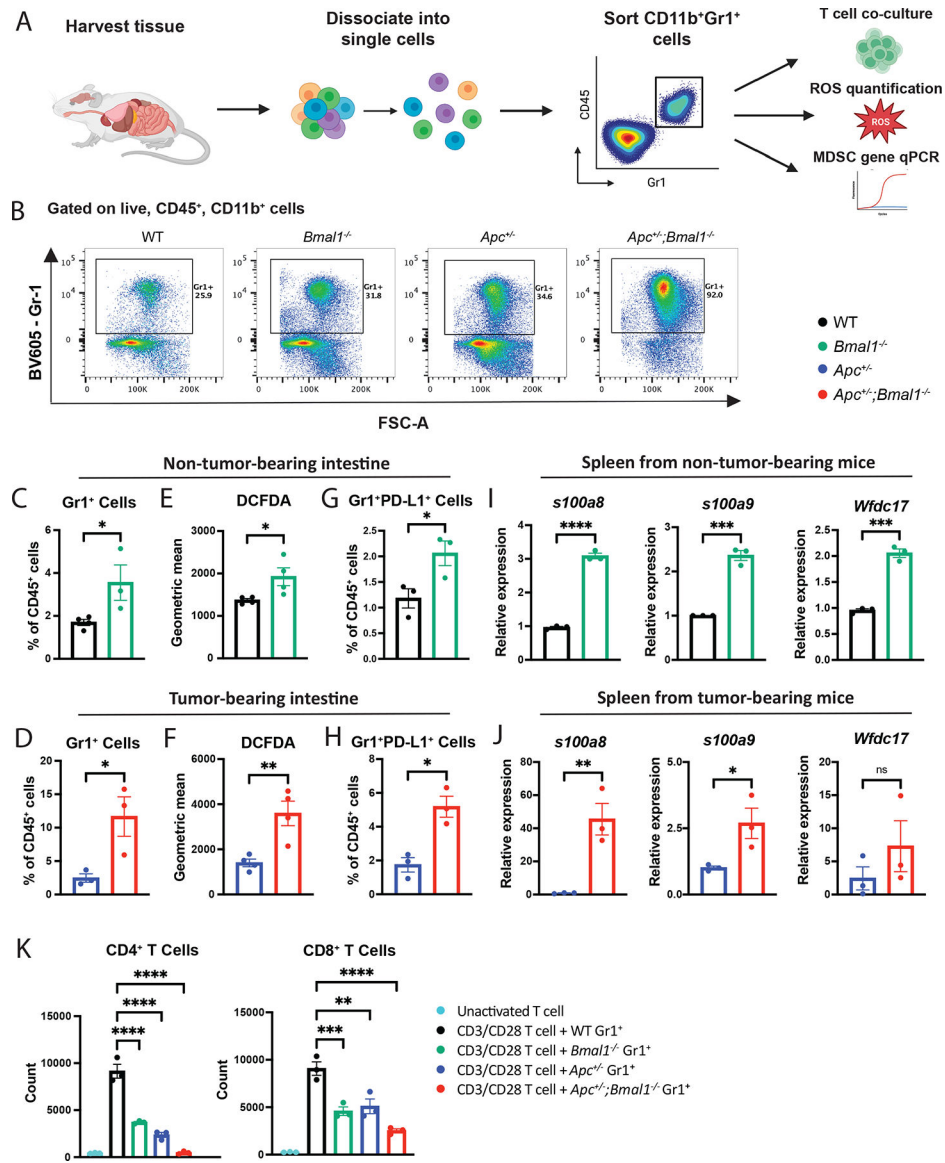
Fig. 3. Disruption of the circadian clock promotes the accumulation of MDSCs.
(A) Schematic depicting workflow for MDSC assays including T cell co-culture and proliferation, reactive oxygen species (ROS) quantification, and MDSC qPCR from live, CD45$^+$CD11b$^+$Gr1$^+$ sorted cells. **(B)** Representative percent of Gr1$^+$ cells after gating for live, CD45$^+$CD11b$^+$ cells from WT, $Bmal1^{-/-}$, $Apc^{+/-}$, and $Apc^{+/-}$;$Bmal1^{-/-}$ small intestine using flow cytometry. **(C-D)** Quantification of Gr1$^+$ cells as percent of CD45$^+$ cells from WT, $Bmal1^{-/-}$, $Apc^{+/-}$, and $Apc^{+/-}$;$Bmal1^{-/-}$ small intestine sacrificed at ZT 4 and analyzed by flow cytometry (n=3 mice/genotype). **(E-F)** Geometric mean of DCFDA from WT, $Bmal1^{-/-}$, $Apc^{+/-}$, and $Apc^{+/-}$;$Bmal1^{-/-}$ small intestine sacrificed at ZT 4 and analyzed by flow cytometry (n=4 mice/genotype). **(G-H)** Gr1$^+$PD-L1$^+$ cells shown as percent of CD45$^+$ cells from WT, $Bmal1^{-/-}$, $Apc^{+/-}$, and $Apc^{+/-}$;$Bmal1^{-/-}$ small intestine sacrificed at ZT 4 and analyzed by flow cytometry (n=3 mice/genotype). **(I-J)** Expression of $s100a8$, $s100a9$, and $Wfdc17$ as determined by qPCR using splenic Gr1$^+$ sorted cells from WT, $Bmal1^{-/-}$,

$Apc^{+/-}$, and $Apc^{+/-}$;$Bmal1^{-/-}$ mice sacrificed at ZT 4 (n=3 mice/genotype). **(K)** Bar graph of CD4$^+$ and CD8$^+$ T cell counts measured by FACS quantification in inactivated T cells or CD3/CD28 activated T cells with a 1:1 ratio of CD11b$^+$Gr1$^+$ cells from WT, $Bmal1^{-/-}$, $Apc^{+/-}$ and $Apc^{+/-}$;$Bmal1^{-/-}$ spleen (n=3 mice/genotype). Data represent the mean ± SEM. Statistical significance was determined by two-tailed Mann-Whitney T-test for C-J, and one-way ANOVA with Tukey's multiple comparison for K. Asterisks represent p-values from multiple comparisons, with * indicating a p-value of < 0.05, ** indicating a p-value of < 0.01, *** indicating a p-value of < 0.001, **** a p-value of < 0.0001, and ns = not significant.
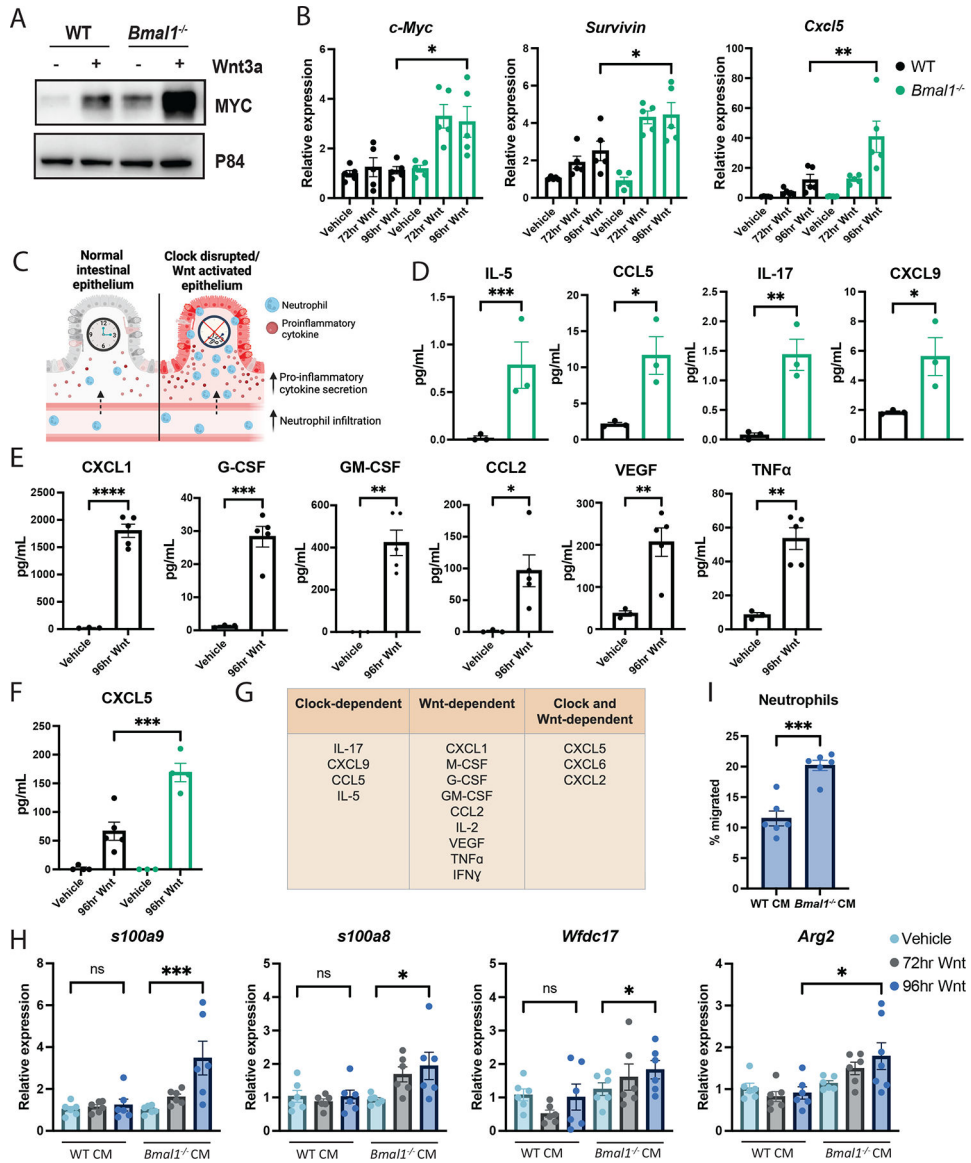
Fig. 4. Circadian clock disruption and Wnt signaling promote an inflammatory response.
(**A**) Western blot of MYC and p84 in WT and *Bmal1*$^{-/-}$ intestinal organoids untreated
or treated with 100 ng/mL recombinant Wnt3a for 72 hours. (**B**) Expression of *c-Myc,
Survivin*, and *Cxcl5* determined by qPCR using WT and *Bmal1*$^{-/-}$ primary intestinal
monolayers untreated or treated with 100 ng/mL recombinant Wnt3a for 72 or 96 hours.
(n=5 independent monolayer lines/genotype). (**C**) Proposed model of normal versus clock
disrupted/Wnt activated intestinal epithelium. (**D**) Concentration of secreted IL-5, CCL5,
IL-17, and CXCL9 in CM from WT and *Bmal1*$^{-/-}$ intestinal monolayers determined by
ELISA (n=3 independent monolayer lines/genotype). (**E**) WT intestinal monolayers were
untreated or treated with 100 ng/mL recombinant Wnt3a for 96 hours (n=3 untreated, n=5
Wnt3a-treated independent monolayer lines/genotype). Concentration of secreted CXCL1,
G-CSF, GM-CSF, CCL2, VEGF, and TNFα was determined by ELISA. (**F**) WT and
Bmal1$^{-/-}$ intestinal monolayers were untreated or treated with 100 ng/mL recombinant

Wnt3a for 96 hours (n=3 untreated, n=4 Wnt3a-treated independent monolayer lines/genotype). Concentration of secreted CXCL5 was determined by ELISA. **(G)** Clock-dependent, Wnt-dependent, and both clock- and Wnt-dependent cytokines determined by ELISA. **(H)** Gene expression of *s100a9, s100a8, Wfdc17*, and *Arg2* determined by qPCR of naïve neutrophils cultured with WT and *Bmal1*$^{-/-}$ intestinal monolayers CM (n=6 independent monolayer lines/genotype). **(I)** Neutrophil migration toward WT and *Bmal1*$^{-/-}$ intestinal monolayers CM (n=6 independent monolayer lines/genotype). Data represent the mean ± SEM. Statistical significance was determined by two-tailed Mann-Whitney T-test for D-E and I, and one-way ANOVA with Tukey's multiple comparison for B, F, and H. Asterisks represent p-values from multiple comparisons, with * indicating a p-value of < 0.05, ** indicating a p-value of < 0.01, *** indicating a p-value of < 0.001, **** a p-value of < 0.0001, and ns = not significant.
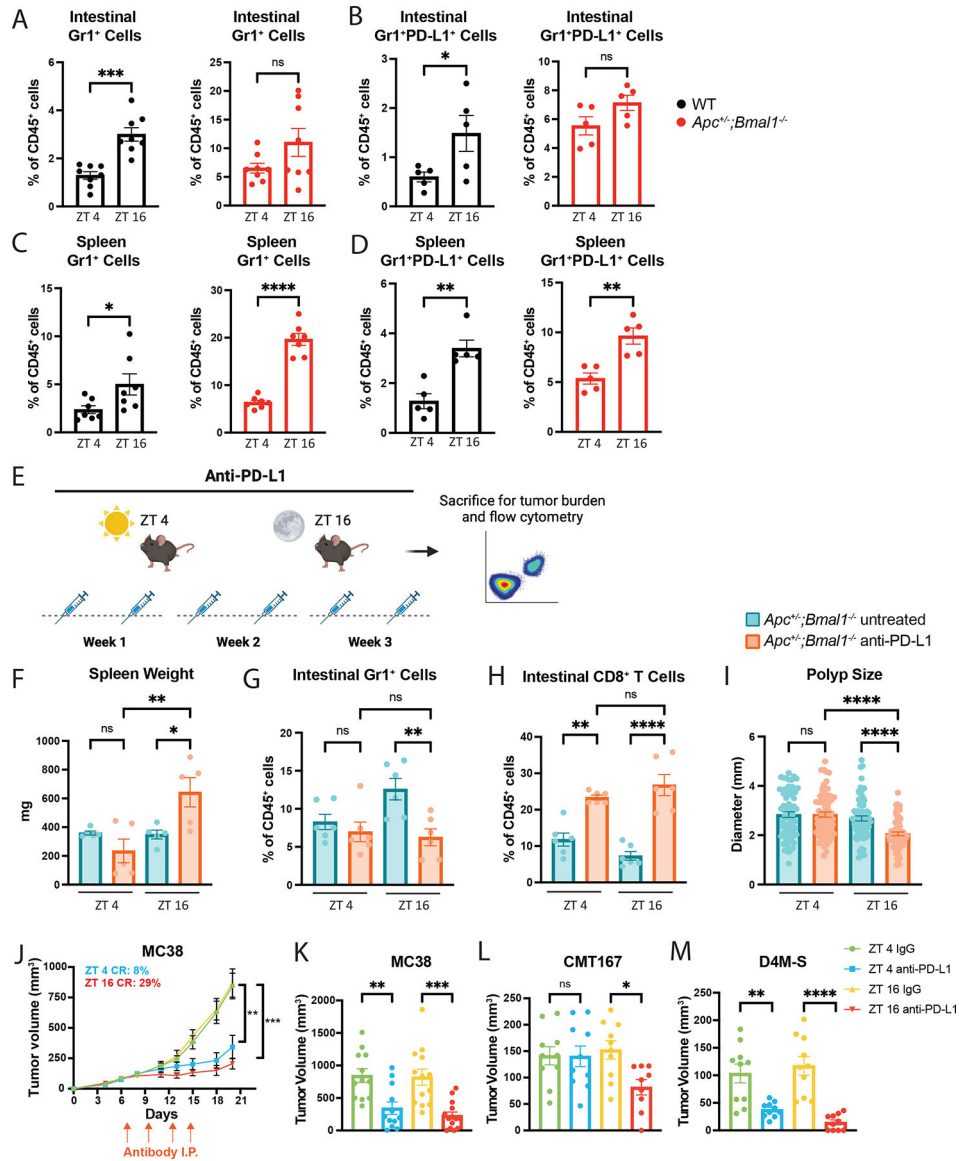
Fig. 5. Time-of-day anti-PD-L1 treatment determines efficacy.
(**A-B**) Small intestinal Gr1+ or Gr1+PD-L1+ cells as percent of CD45+ cells from WT and $Apc^{+/-};Bmal1^{-/-}$ mice (n=5 mice/group for A and 8 mice/group for B). (**C-D**) Splenic Gr1+ or Gr1+PD-L1+ cells as percent of CD45+ cells from WT and $Apc^{+/-};Bmal1^{-/-}$ mice (n=5 mice/genotype for C, n=7 mice/genotype for D). For A-D, animals were sacrificed at ZT 4 and ZT 16 and analyzed by flow cytometry. (**E**) Graphical schematic of anti-PD-L1 administration experiment at two circadian time points. (**F**) Spleen weight of $Apc^{+/-};Bmal1^{-/-}$ mice untreated or treated with anti-PD-L1 at ZT 4 or ZT 16 (n=5 mice/group). (**G-H**) Small intestinal Gr1+ cells or CD8+ T cells as percent of CD45+ cells from $Apc^{+/-};Bmal1^{-/-}$ mice untreated or treated with anti-PD-L1 at ZT 4 or ZT 16 and analyzed by flow cytometry (n=6 mice/group). (**I**) Small intestinal polyp size from $Apc^{+/-};Bmal1^{-/-}$ mice untreated or treated with anti-PD-L1 at ZT 4 or ZT 16 (n=70 polyps/group). (**J**) Tumor volume over time for WT mice after subcutaneous injection of MC38 cells and treatment

with IgG or anti-PD-L1 at ZT 4 or ZT 16 (n=7 mice/group). **(K)** Tumor volume of WT mice 21 days after subcutaneous injection of MC38 cells and treatment with IgG or anti-PD-L1 at ZT 4 or ZT 16 (n=7 mice/group, 2 tumors/mouse). **(L)** Tumor volume of WT mice 18 days after subcutaneous injection of CMT167 cells and treatment with IgG or anti-PD-L1 at ZT 4 or ZT 16 (n=5 mice/group, 2 tumors/mouse). **(M)** Tumor volume of WT mice 12 days after subcutaneous injection of D4M-S cells and treatment with IgG or anti-PD-L1 at ZT 4 or ZT 16 (n=5 mice/group, 2 tumors/mouse). Data represent the mean ± SEM. Statistical significance was determined by two-tailed Mann-Whitney T-test for A-D, one-way ANOVA with Tukey's multiple comparison for F-I and K-M, and two-way ANOVA with Tukey's multiple comparison for J. Asterisks represent p-values from multiple comparisons, with * indicating a p-value of < 0.05, ** indicating a p-value of < 0.01, *** indicating a p-value of < 0.001, **** indicating a p-value of < 0.0001, and ns = not significant.
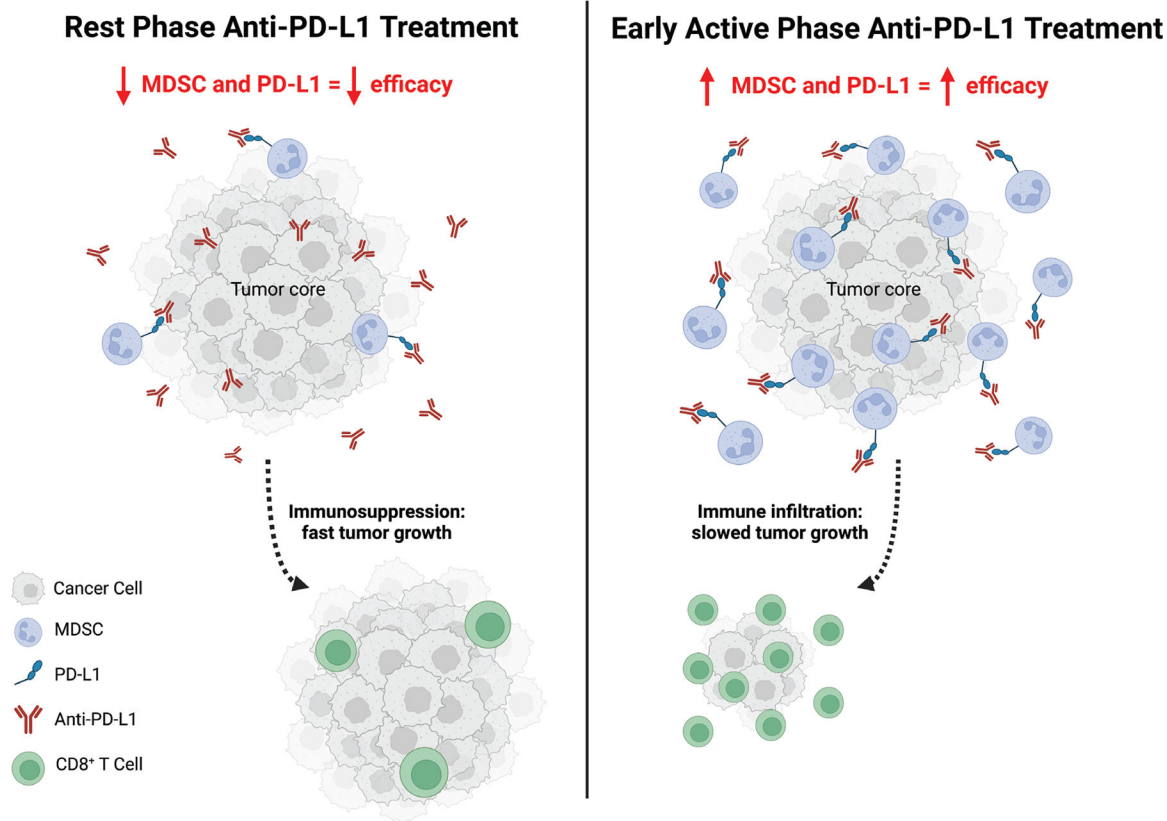
Fig. 6. Model depicting circadian regulation of MDSCs for anti-PD-L1 treatment.
MDSC abundance and PD-L1 expression is regulated by the circadian clock with a peak during the early active phase. By treating with anti-PD-L1 during the early active phase, when PD-L1 expressing MDSCs are most abundant, immune infiltration is stimulated and tumor growth is inhibited. Figure created using biorender.com.

Table 1.

List of primers used for gene expression analysis.

Mouse qPCR Primer Name	Primer Sequence (5' to 3')
18S mRNA Fwd	CGCCGCTAGAGGTGAAATTC
18S mRNA Rev	CGAACCTCCGACTTTCGTTCT
S100a8 mRNA Fwd	GTCCTCAGTTTGTGCAGAATATAAA
S100a8 mRNA Rev	TTTGTGAGATGCCACACCCA
S100a9 mRNA For	TGGCAACCTTTATGAAGAAAGAGAA
S100a9 mRNA Rev	GCCATCAGCATCATACACTCC
Wfdc17 mRNA For	TTTGATCACTGTGGGGATG
Wfdc17 mRNA Rev	ACACTTTCTGGTGAAGGCTTG
Arg2 mRNA For	AGGAGTGGAATATGGTCCAGC
Arg2 mRNA Rev	AGGGATCATCTTGTGGGACATT
c-Myc mRNA For	AGCTCGCCCAAATCCTGTAC
c-Myc mRNA Rev	TTGTGCTGGTGAGTGGAGAC
Survivin mRNA For	GAACCCGATGACAACCCGAT
Survivin mRNA Rev	TTGGCTCTCTCTGTCTGTCCAG
Cxcl5 mRNA For	GAGCTGCGTTGTGTTTGCTT
Cxcl5 mRNA Rev	TAGCTTTCTTTTTGTCACTGCCC
Cxcl1 mRNA For	CCAGACTTGAAGGTGTTGC
Cxcl1 mRNA Rev	TCTGAACCAAGGGAGCTTCA
M-csf mRNA For	AGTGGAAGTGGAGGAGCCAT
M-csf mRNA Rev	TGGTGAGGGGTCATAGAATCC
Gm-csf mRNA For	GGCCTTGGAAGCATGTAGAG
Gm-csf mRNA Rev	CCGTAGACCCTGCTCGAATA
Axin2 mRNA For	TGTCCTGGGGGAACAGATTA
Axin2 mRNA Rev	TTTTGGCAAGGTACCACCTC